

1 **Reply to Referee #1's comments:**

2  
3 We thank Referee #1 for the review and very useful suggestions. Our responses are itemized  
4 below.

5  
6 *“General. This study explored the ozone-CO correlations on the global scale in boreal summer*  
7 *using a chemical transport model (Global Modeling Initiative (GMI)), driven by three sets of*  
8 *meteorological data: fvGCM with sea surface temperature for 1995, GEOS4-DAS for 2005, and*  
9 *MERRA for 2005. The simulations are compared with the measurements from the Tropospheric*  
10 *Emission Spectrometer (TES) satellite instrument so the model’s capability to reproduce the TES*  
11 *data and sensitivity to various meteorological data were examined. Three radionuclide tracers*  
12 *were simulated as proxies for various transport-related processes to help untangle the simulated*  
13 *ozone-CO correlations and explain the differences. Sensitivity of ozone-CO correlations to*  
14 *various emissions was tested with GMI-MERRA simulations. This study has addressed an*  
15 *important issue in atmospheric chemistry. The paper is well written with logic flow of text, clear*  
16 *description of the method and assumptions, proper and adequate literature review, and high*  
17 *quality of figures. This study is novel and solid. It offers new insight on global ozone-CO*  
18 *correlations and underlying mechanisms.”*

19  
20 **Reply** – Thanks for the comments.

21  
22 *“Specific. While GMI simulates tropospheric ozone reasonably well, it underestimates*  
23 *tropospheric CO as suggested in this and earlier studies. This underestimation may cause some*  
24 *biases for the ozone-CO correlations presented in this study. Please discuss.”*

25  
26 **Reply** – Good point. We have revised the first paragraph of Section 5 (P19): “In this section, we  
27 examine O<sub>3</sub> and CO relationships at 618hPa in GMI CTM. We interpret GMI simulated O<sub>3</sub>-CO  
28 correlations and their slopes in the context of emissions, photochemical transformation, and  
29 transport (e.g., convection, STE, and large-scale subsidence), using model meteorological data  
30 and radionuclide simulations. We then evaluate them with those derived from TES satellite  
31 observations. Note that the model underestimate of CO concentrations does not significantly  
32 affect the calculated O<sub>3</sub>-CO correlations although it may cause biases in the regression slopes  
33 due to the association of the latter with ozone production efficiency”.

1

2 *“In the model simulations, the anthropogenic emissions are kept the same (using 2005’s*  
3 *emissions) for the simulations driven by the three sets of meteorological data. The surface*  
4 *biomass and biogenic emissions are all the same for the three simulations. Therefore, the*  
5 *differences seen in the three simulations are due to different meteorological fields that also cause*  
6 *the differences in lightning emissions. As understandable, the authors placed their focus on the*  
7 *middle troposphere when comparing GMI and TES results because TES data are least biased at*  
8 *these altitudes (Figures 12-15). Therefore, showing NOX emissions from lightning in the middle*  
9 *troposphere horizontally (like Figure 9) would help interpret Figures 12-15.”*

10

11 **Reply** – As discussed on P15 (L15-20, Table 1), all simulations show similar lightning NO<sub>x</sub>  
12 (LNO<sub>x</sub>) emissions during July-August. However, GMI/fvGCM shows a factor of ~ 2.5 lower  
13 LNO<sub>x</sub> emissions than GMI/GEOS4 and GMI/MERRA during May-June. The July-August LNO<sub>x</sub>  
14 emissions do not explain the discrepancy in the simulated ozone, and therefore we decide not to  
15 add a plot of LNO<sub>x</sub> emissions. We have added a sentence in the text (P15) as below: “It is noted  
16 that all simulations show hot spots of LNO<sub>x</sub> emissions over the central and eastern US, central  
17 Africa, and west Tibetan plateau (not shown).”

18

19 *“For the model validation (Figure 6), please provide the values of correlation coefficients, mean*  
20 *biases, and root mean square error so to help evaluate the performance of each simulation*  
21 *quantitatively (in the figure or in a table).”*

22

23 **Reply** – Thanks for the suggestion. We have added a new table (Table 2) and a sentence in the  
24 text (P15): “The mean differences between simulated O<sub>3</sub> and ozonesonde observations at 500  
25 hPa (MT) and 200 hPa (UT), respectively, are listed in Table 2.”

26

27 *“Page 2, Line 13, the authors claimed the simulated ozone-CO correlation patterns are consistent*  
28 *with those derived from TES observations, except in the tropical easterly biomass burning*  
29 *outflow regions. This claim is not be fully supported by Figures 13 and 14. There are large*  
30 *regions with negative correlations in the simulations that are not shown in the TES data. There*  
31 *are other discernible discrepancies between TES and GMI data that should be mentioned and*  
32 *discussed.”*

33

1 **Reply** – Thanks for pointing this out. We have revised the text to “Despite the fact that the three  
2 simulations show significantly different global and regional distributions of O<sub>3</sub> and CO  
3 concentrations, they show similar patterns of O<sub>3</sub>-CO correlations on a global scale. All model  
4 simulations sampled along the TES orbit track capture the observed positive O<sub>3</sub>-CO correlations  
5 in the Northern Hemisphere mid-latitude continental outflow and the Southern Hemisphere  
6 subtropics. While all simulations show strong negative correlations over the Tibetan Plateau,  
7 northern Africa, northern subtropical eastern Pacific, and Caribbean, TES O<sub>3</sub> and CO  
8 concentrations at 618 hPa only show weak negative correlations over much narrower areas (i.e.,  
9 the Tibetan Plateau and northern Africa). Discrepancies in regional O<sub>3</sub>-CO correlation patterns in  
10 the three simulations may be attributed to differences in convective transport, stratospheric  
11 influence, and subsidence, among other processes.”

12

13 *“Page 21, Line 3-4: The authors stated: “Strong positive O<sub>3</sub>-CO correlations are present in all*  
14 *simulations at 618 hPa over Indonesia (Figure 12)”. Over the entire Indonesia? The positive*  
15 *correlations appear only over western Indonesia where simulations show high CO.”*

16

17 **Reply** – Indeed. We have revised the sentence to “Strong positive O<sub>3</sub>-CO correlations are  
18 present in all simulations at 618 hPa over western and central Indonesia (Figure 12), reflecting  
19 convective transport of biomass burning CO (Figure 8) and photochemical production of O<sub>3</sub>  
20 from its precursors.”

21

22 *“Remove an extra comma near the ends for Luo et al. (2007 a and b) and Mao, H., and*  
23 *Talbot, R. (2004) in References.”*

24

25 **Reply** – Done.

26

27

28 *“Word “Figure” may not be in bold in the final version.”*

29

30 **Reply** – Corrected.

31

1  
2  
3  
4  
5  
6  
7  
8  
9  
10  
11  
12  
13  
14  
15  
16  
17  
18  
19  
20  
21  
22  
23  
24  
25  
26  
27  
28  
29  
30  
31  
32

**Reply to Dr. Vincent Huijnen’s comments:**

We thank Dr. Vincent Huijnen for very helpful comments. Our responses are itemized below.

*“General comments. This is a very well written manuscript describing a thorough analysis of the model O3-CO correlations in the free troposphere, as a means to analyze origins of model biases. The authors analyze various meteorological drivers, and the relative contribution of different emission sources to the modeled correlations, and evaluate them against TES observations at 618hPa. Overall I have very few comments, hence I recommend this manuscript for publication.”*

*“Specific comments. In the manuscript I miss a comment regarding the spinup-time of the individual model runs.*

**Reply** – Thanks for pointing this out. Now we state in the text: “All standard and perturbation full-chemistry simulations for July-August as presented in this paper were conducted with a 6-month spinup.” (Section 2.1.1), and “All simulations of radionuclide tracers were conducted with a 5-year spinup in order for <sup>210</sup>Pb to reach an equilibrium in the stratosphere.” (Section 2.1.3).

*“Also for GMI/fvGCM you use meteorology from the year 1995, while for the other two simulations you take 2005 meteorology. Did you analyze any potential systematic differences between these two years? I understand this has no impact on the general conclusions drawn from this work.”*

**Reply** – We did not examine any potential systematic differences between 1995 and 2005 meteorology. GMI/fvGCM was driven with the output from the fvGCM general circulation model (with sea surface temperature for 1995), which was intended to represent only the contemporary climatological state of the atmosphere. Indeed, this does not affect the general conclusion of this study. We have modified the text (P 9) to: “We drive the GMI CTM with three meteorological datasets from: the free-running NASA Global Modeling and Assimilation Office (GMAO) finite-volume General Circulation Model (fvGCM with sea surface temperature for

1 1995), the Goddard Earth Observing System Data Assimilation System Version 4 (GEOS4-  
2 DAS) for 2005, and the Modern-Era Retrospective Analysis for Research and Applications  
3 (MERRA) for 2005.”

4

5 *“The authors analyze the impact of three meteorological drivers. Here I think it would be very*  
6 *interesting if they would have included, or will include in future work, ECMWF-based*  
7 *meteorology (ERA-Interim) in their analysis.”*

8

9 **Reply** – Indeed, it would be very interesting to include the ERA-Interim meteorology in future  
10 work. Now we state in the text (P32-33): “Future work, where additional meteorological  
11 archives (e.g., GFDL AM3, ECMWF ERA-Interim) may also be incorporated, should examine  
12 the driving factors for O<sub>3</sub>-CO correlations in other seasons.”

13

14 *“The authors blame an over-estimate of O3 in the SH subtropics in GMI/MERRA due to too*  
15 *shallow tropical deep convection. Even though the contribution of this process is clearly*  
16 *illustrated by the 222Rn-based analysis, I wonder if the conclusion is correct: is there a*  
17 *possibility of compensating errors? Is there independent evidence that MERRA tropical deep*  
18 *convection is too shallow?”*

19

20 **Reply** – Point well taken. This overestimate also involves factors other than too shallow tropical  
21 deep convection, for which we did not find independent evidence. We have revised the statement  
22 in the Conclusion section to: “Among the three GMI simulations, GMI/GEOS4-simulated O<sub>3</sub>  
23 concentrations are in best agreement with the observations. GMI/MERRA underestimates O<sub>3</sub> in  
24 the NH high-latitude UT due to weak STE, and overestimates O<sub>3</sub> in the SH subtropics. The latter  
25 is due to a combination of excessive influences from lightning NO<sub>x</sub> emissions and STE (or  
26 subsidence), as well as the shallower convection resulting in less low-O<sub>3</sub> air lifted from the LT to  
27 MT/UT.”

28

29 *“The authors also analyze the contribution of STE to tropospheric O3. Here, it would be useful*  
30 *to see budget numbers of their (annual mean) STE, to be able to intercompare with other*  
31 *systems.”*

32

1 **Reply** – Unfortunately, our model analysis focused on July-August and the annual mean STE  
2 fluxes of ozone are not available.

3

4 *“Technical corrections. Pp11, l i ne 10: The tropopause...; Pp17, line 13: ...previously*  
5 *suggested that the O3 maximum...; Pp19, line 12: ...found a multi-mode l...; Pp29, l i ne 23:*  
6 *...simulated ~~in~~ downwind ...”*

7

8 **Reply** – Corrected.

9

10

11

**Revised text with track changes**

12

**(next page)**

13

14

15

16

17

18

19

20

21

22

23

1 **Global O<sub>3</sub>-CO Correlations in a Chemistry and Transport**  
2 **Model during July–August: Evaluation with TES Satellite**  
3 **Observations and Sensitivity to Input Meteorological Data**  
4 **and Emissions**

5  
6 Hyun-Deok Choi<sup>1</sup>, Hongyu Liu<sup>1</sup>, James H. Crawford<sup>2</sup>, David B. Considine<sup>2,3</sup>, Dale J.  
7 Allen<sup>4</sup>, Bryan N. Duncan<sup>5</sup>, Larry W. Horowitz<sup>6</sup>, Jose M. Rodriguez<sup>5</sup>, Susan E. Strahan<sup>5,7</sup>,  
8 Lin Zhang<sup>8,9</sup>, Xiong Liu<sup>8</sup>, Megan R. Damon<sup>5,10</sup>, and Stephen D. Steenrod<sup>5,7</sup>

9  
10 <sup>1</sup>National Institute of Aerospace, Hampton, VA

11 <sup>2</sup>NASA Langley Research Center, Hampton, VA

12 <sup>3</sup>Now at NASA Headquarters, Washington, D.C.

13 <sup>4</sup>University of Maryland, College Park, MD

14 <sup>5</sup>NASA Goddard Space Flight Center, Greenbelt, MD

15 <sup>6</sup>NOAA Geophysical Fluid Dynamics Laboratory, Princeton, NJ

16 <sup>7</sup>Universities Space Research Association, Columbia, MD

17 <sup>8</sup>Harvard University, Cambridge, MA

18 <sup>9</sup>Now at Peking University, Beijing, China

19 <sup>10</sup>Science Systems and Applications, Inc., Lanham, MD

20

21 *Atmos. Chem. Phys.*, **revised, May 2017**

22

23 **Correspondence:**

24

25 Hongyu Liu

26 Chemistry and Dynamics Branch, Mail Stop 401B

27 NASA Langley Research Center, Hampton, VA 23681

28 Tel: 757-864-3191; Email: [Hongyu.Liu-1@nasa.gov](mailto:Hongyu.Liu-1@nasa.gov)

29

Deleted: Submitted to

Deleted: 2

Deleted: 6

1 **Abstract.** We examine the capability of the Global Modeling Initiative (GMI) chemistry and  
2 transport model to reproduce global mid-tropospheric (618hPa) O<sub>3</sub>-CO correlations determined by  
3 the measurements from Tropospheric Emission Spectrometer (TES) aboard NASA's Aura satellite  
4 during boreal summer (July–August). The model is driven by three meteorological data sets  
5 (fvGCM with sea surface temperature for 1995, GEOS4-DAS for 2005, and MERRA for 2005),  
6 allowing us to examine the sensitivity of model O<sub>3</sub>-CO correlations to input meteorological data.  
7 Model simulations of radionuclide tracers (<sup>222</sup>Rn, <sup>210</sup>Pb, and <sup>7</sup>Be) are used to illustrate the  
8 differences in transport-related processes among the meteorological data sets. Simulated O<sub>3</sub> values  
9 are evaluated with climatological ozone profiles from ozonesonde measurements and satellite  
10 tropospheric O<sub>3</sub> columns. Despite the fact that the three simulations show significantly different  
11 global and regional distributions of O<sub>3</sub> and CO concentrations, they show similar patterns of O<sub>3</sub>-  
12 CO correlations on a global scale. All model simulations sampled along the TES orbit track capture  
13 the observed positive O<sub>3</sub>-CO correlations in the Northern Hemisphere mid-latitude continental  
14 outflow and the Southern Hemisphere subtropics. While all simulations show strong negative  
15 correlations over the Tibetan Plateau, northern Africa, northern subtropical eastern Pacific, and  
16 Caribbean, TES O<sub>3</sub> and CO concentrations at 618 hPa only show weak negative correlations over  
17 much narrower areas (i.e., the Tibetan Plateau and northern Africa). Discrepancies in regional O<sub>3</sub>-  
18 CO correlation patterns in the three simulations may be attributed to differences in convective  
19 transport, stratospheric influence, and subsidence, among other processes. To understand how  
20 various emissions drive global O<sub>3</sub>-CO correlation patterns, we examine the sensitivity of  
21 GMI/MERRA model-calculated O<sub>3</sub> and CO concentrations and their correlations to emission types  
22 (fossil fuel, biomass burning, biogenic, and lightning NO<sub>x</sub> emissions). Fossil fuel and biomass  
23 burning emissions are mainly responsible for the strong positive O<sub>3</sub>-CO correlations over

**Deleted:** all simulations

**Deleted:** These patterns are consistent with those derived from TES observations, except in the tropical easterly biomass burning outflow regions.

**Formatted:** Font: Bold

1 continental outflow regions in both hemispheres. Biogenic emissions have a relatively smaller  
2 impact on O<sub>3</sub>-CO correlations than other emissions, but are largely responsible for the negative  
3 correlations over the tropical eastern Pacific, reflecting the fact that O<sub>3</sub> is consumed and CO  
4 generated during the atmospheric oxidation process of isoprene under low NO<sub>x</sub> conditions. We  
5 find that lightning NO<sub>x</sub> emissions degrade both positive correlations at mid-/high- latitudes and  
6 negative correlations in the tropics because ozone production downwind of lightning NO<sub>x</sub>  
7 emissions is not directly related to the emission and transport of CO. Our study concludes that O<sub>3</sub>-  
8 CO correlations may be used effectively to constrain the sources of regional tropospheric O<sub>3</sub> in  
9 global 3-D models, especially for those regions where convective transport of pollution plays an  
10 important role.

11

## 12 **1. Introduction**

13 Ozone (O<sub>3</sub>) is an important greenhouse gas in the troposphere and a pollutant at the surface.  
14 It is a primary source of the hydroxyl radical (OH), which controls the oxidizing power of the  
15 troposphere. Ozone in the troposphere is produced by photochemical oxidation of carbon  
16 monoxide (CO), methane, and volatile organic hydrocarbons (VOCs) in the presence of nitrogen  
17 oxides (NO<sub>x</sub> ≡ NO + NO<sub>2</sub>). Its precursors are emitted by human activity (e.g., fossil fuel  
18 combustion and industrial processes), biomass burning, vegetation, soils, and lightning. Ozone is  
19 also transported down from the stratosphere by the Brewer Dobson circulation. Carbon monoxide  
20 is a product of incomplete combustion. Its sources include fossil fuel and biofuel combustion,  
21 biomass burning, and chemical production from atmospheric oxidation of methane, isoprene, and  
22 other VOCs. Its primary sink is reaction with OH.

1            Since CO is a precursor of tropospheric O<sub>3</sub> and an excellent tracer for long-range transport  
2 of pollution owing to its tropospheric lifetime of a few months, correlations between O<sub>3</sub> and CO  
3 are useful indicators of the efficiency of O<sub>3</sub> production and export (e.g., Parrish et al., 1993; Mao  
4 and Talbot, 2004). Generally, a positive correlation in summer indicates strong photochemical  
5 production of O<sub>3</sub> downwind of polluted regions (Chin et al., 1994; Tsutsumi and Matsueda, 2000).  
6 A negative correlation indicates stratospheric influence (Parrish et al., 1998; Hsu et al., 2004),  
7 photochemical O<sub>3</sub> destruction (Fishman and Seiler, 1983; Parrish et al., 1998; Mao and Talbot,  
8 2004), or chemical production of CO (Chin et al., 1994; Real et al., 2008). Small correlation  
9 coefficients and small linear regression slopes are indications of fresh pollution plumes that have  
10 not yet realized their O<sub>3</sub> production potential due to, for example, incomplete photochemical  
11 processes (Naja et al., 2003).

12            Many studies have used surface and/or aircraft observed O<sub>3</sub>-CO correlations to understand  
13 anthropogenic influences on O<sub>3</sub>, especially in the Northern Hemisphere (NH) continental outflow  
14 regions such as the northeastern US/northern Atlantic (Fishman and Seiler, 1983; Anderson et al.,  
15 1993; Parrish et al., 1993; Chin et al., 1994; Fehsenfeld et al., 1996; Parrish et al., 1998; Li et al.,  
16 2002; Honrath et al., 2004; Mao and Talbot, 2004) and the Asian Pacific Rim (Tsutsumi and  
17 Matsueda, 2000; Mauzerall et al., 2000). The studies found strong O<sub>3</sub>-CO correlations in outflow  
18 regions and concluded that the export of pollution from the NH major continents makes a  
19 significant contribution to total tropospheric O<sub>3</sub> over the NH during summer.

20            The observed O<sub>3</sub>-CO correlation coefficients and linear regression slopes have been used  
21 to evaluate the capability of models of chemistry and transport to produce proper O<sub>3</sub> levels from  
22 its precursors for the right reasons (e.g., Chin et al., 1994; Mauzerall et al., 2000; Zhang et al.,  
23 2006; Voulgarakis et al., 2011). Shim et al. (2009) examined the Mexico City pollution outflow

1 using O<sub>3</sub>, CO, and their correlations from TES as well as aircraft measurements obtained during  
2 the Megacity Initiative: Local and Global Research Observations (MILAGRO) / Intercontinental  
3 Chemical Transport Experiment (INTEX-B) campaigns. These investigations found that TES data  
4 is characterized by smaller O<sub>3</sub>-CO correlation coefficients but larger linear regression slopes than  
5 *in situ* observations at 618 hPa partly due to the lack of variability in TES CO. Two previous  
6 studies also examined TES global O<sub>3</sub>-CO correlations. Zhang et al. (2006) compared mid-  
7 tropospheric TES O<sub>3</sub>-CO correlations in July 2005 over the eastern United States with those from  
8 the GEOS-Chem model and International Consortium for Atmospheric Research on Transport and  
9 Transformation (ICARTT) aircraft observations (July 2004), finding that TES can provide good  
10 information on global mid-tropospheric O<sub>3</sub>-CO correlations. Voulgarakis et al. (2011) expanded  
11 the scope of Zhang et al. (2006), evaluating O<sub>3</sub>-CO correlations simulated by two independent  
12 models against five years of TES observations. They suggested that in addition to O<sub>3</sub>  
13 photochemical processes, transport may also play an important role in the O<sub>3</sub>-CO correlations.  
14 However, Voulgarakis et al. (2011) could not isolate the effect of transport because the two models  
15 in their study used different input meteorological data sets as well as different chemical and  
16 transport mechanisms.

17 In this paper, we present O<sub>3</sub> and CO simulations using the Global Modeling Initiative  
18 (GMI) chemistry and transport model (CTM) driven by three meteorological data sets. The model  
19 can incorporate different inputs and components (e.g., meteorological fields, emission inventories,  
20 and chemical mechanisms), allowing us to test the sensitivity of model simulations to input  
21 meteorological data sets (e.g., Douglass et al., 1999; Considine et al., 2005; Liu et al., 2016). Model  
22 simulations are evaluated using ozonesonde and satellite observations. We then test the model's  
23 capability to reproduce the mid-tropospheric O<sub>3</sub>-CO correlations determined from TES

1 measurements. We present the differences in the simulated O<sub>3</sub>-CO correlations due to the use of  
2 different meteorological input data, and interpret those differences in terms of transport using  
3 radionuclide species (<sup>222</sup>Rn, <sup>210</sup>Pb, and <sup>7</sup>Be) as tracers of atmospheric transport (see Section 2.1.3).  
4 We also investigate the effect of emission types on O<sub>3</sub> and CO concentrations and their correlations  
5 in the model.

6 This paper is organized as follows. Section 2: Descriptions of the GMI model,  
7 meteorological data sets, and observational data sets. Section 3: Presentation of the model  
8 simulations of radionuclides, O<sub>3</sub> and CO. Section 4: Evaluation of GMI O<sub>3</sub> and CO simulations  
9 with observations. Section 5: Evaluation of GMI O<sub>3</sub>-CO correlations with satellite observations  
10 from TES. Section 6: Analysis of the effects of various emission types on the model simulated O<sub>3</sub>-  
11 CO correlations. Section 7: Summary and conclusions.

12

## 13 **2. Model and Data**

### 14 **2.1. GMI**

#### 15 **2.1.1. The CTM**

16 The GMI CTM is a global 3-D composition model that combines both tropospheric and  
17 stratospheric chemical mechanisms, including 124 species, 322 chemical reactions, and 81  
18 photolysis reactions (Ziemke et al, 2006; Duncan et al., 2007a; Considine et al., 2008; Allen et al.,  
19 2010). The tropospheric mechanism includes a detailed description of tropospheric O<sub>3</sub>-NO<sub>x</sub>-  
20 hydrocarbon chemistry (Bey et al., 2001) with recent updates (e.g., see Allen et al., 2010). The  
21 stratospheric mechanism is described in Kinnison et al. (2001) and Douglass et al. (2004). The

1 details of the GMI model are described in Duncan et al. (2007a) and Strahan et al. (2007). The  
2 basic structure of the model is described in Rotman et al. (2001).

3         The GMI model uses a flux-form semi-Lagrangian (FFSL) advection scheme (Lin and  
4 Rood, 1996) and also includes parameterizations of convection, wet scavenging, dry deposition,  
5 and planetary boundary layer mixing. The anthropogenic emission (e.g., fossil fuel emissions)  
6 scheme is from Bey et al. (2001), Benkovitz et al. (1996), and Duncan et al. (2007b). We use the  
7 anthropogenic emission inputs for 2005 for all simulations in this study. The biogenic emission  
8 scheme is calculated online based on Guenther et al. (2006) and biofuel emissions are estimated  
9 from the inventory and emission factors of Yevich and Logan (2003). Biomass burning emissions  
10 are from Duncan et al. (2003) climatology, where the spatial and seasonal variability are derived  
11 from satellite observations of monthly total fire counts. Lightning NO<sub>x</sub> emissions are calculated  
12 locally in deep convection events with the scheme of Allen et al. (2010) where flash rates are  
13 assumed to be proportional to the square of upward convective mass flux but constrained by  
14 monthly average climatological flash rates from V2.2 of the Optical Transient Detector and the  
15 Lightning Imaging Sensor (OTD/LIS) climatology. GMI uses modules developed at Harvard  
16 University to calculate wet scavenging (Mari et al., 2000; Liu et al., 2001) and dry deposition rates  
17 (Jacob and Wofsy, 1990).

18         Several studies have previously evaluated the GMI CTM simulations of tropospheric O<sub>3</sub>  
19 and CO. Ziemke et al. (2006) compared the tropospheric ozone columns (TOC) in an earlier  
20 version of the GMI CTM, which was driven by the fvGCM meteorological fields (details in Section  
21 2.1.2), with those determined from Ozone Monitoring Instrument/Microwave Limb Sounder  
22 (OMI/MLS) measurements from the NASA Aura satellite. The comparison showed similarities  
23 with respect to zonal and seasonal variations of TOC, but the model overestimated TOC over

1 northern Africa by as much as 10 DU, likely due to desert dust effects while underestimating TOC  
2 over the western Pacific warm pool by up to 10 DU. Chandra et al. (2009) evaluated GMI TOC  
3 when driven by the GEOS4 meteorological fields (see Section 2.1.2) with OMI/MLS TOC and  
4 found the model overestimated TOC by 5-10 DU for the latitude band 30°N - 35°N all the year  
5 and over east China in winter and spring when stratosphere-troposphere exchange (STE) is greatest.  
6 Duncan et al. (2008) showed that the annual average surface O<sub>3</sub> concentrations in the GMI/GEOS4  
7 simulation had a high bias of about 11%, with higher biases in summer when photochemical  
8 production is the dominant source of O<sub>3</sub>. Considine et al. (2008) examined the ability of  
9 GMI/fvGCM (4° × 5°) to represent the observed near-tropopause O<sub>3</sub> distributions and found that  
10 annual mean O<sub>3</sub> concentrations were biased high by 45% at the model thermal tropopause likely  
11 due to insufficient vertical resolution near the tropopause (~ 1.1 km) and/or too high vertical  
12 diffusivity.

13 For CO, Duncan et al. (2007a) compared GMI/fvGCM simulated tropospheric CO  
14 concentrations with NOAA Global Monitoring Division (GMD) surface observations. They  
15 showed that the model was biased low at most sites in local winter/spring likely due to  
16 overestimation of OH in the simulation when the CO burden is typically at an annual maximum.  
17 Schoeberl et al. (2006) showed that GMI/fvGCM was able to reproduce the upper  
18 troposphere/lower stratosphere (UT/LS) CO tape recorder caused by seasonal changes in biomass  
19 burning, as identified with the MLS data.

#### 20 **2.1.2. fvGCM, GEOS4, and MERRA Meteorological Data Sets**

21 We drive the GMI CTM with three meteorological datasets from: the free-running NASA  
22 Global Modeling and Assimilation Office (GMAO) finite-volume General Circulation Model

1 (fvGCM with sea surface temperature for 1995), the Goddard Earth Observing System Data  
2 Assimilation System Version 4 (GEOS4-DAS) for 2005, and the Modern-Era Retrospective  
3 Analysis for Research and Applications (MERRA) for 2005. Note that the fvGCM is the general  
4 circulation model in the assimilation system used to generate GEOS4-DAS (Bloom et al., 2005).  
5 The native vertical coordinate of fvGCM and GEOS4-DAS models is a generalized hybrid sigma-  
6 pressure coordinate system with 55 vertical layers and a smooth transition between sigma in the  
7 troposphere (pressure > 200 hPa) and pure pressure in the stratosphere (top pressure 0.01 hPa).  
8 MERRA is a NASA atmospheric reanalysis data set from a new version of GEOS-DAS Version 5  
9 (GEOS-5.2.0). GEOS-5 is a system of models integrated using the Earth System Modeling  
10 Framework (ESMF). Compared to GEOS-4, GEOS-5 adopts an analysis system developed jointly  
11 with the National Centers for Environmental Prediction (NCEP) and a different set of physics  
12 packages for the atmospheric GCM. MERRA has 72 vertical levels with a lid at 0.01 hPa (sigma-  
13 pressure coordinate interface at ~177 hPa). The native horizontal resolution of all meteorological  
14 data sets is  $1^\circ \times 1.25^\circ$ . To improve computational efficiency, we drive GMI CTM with the  
15 meteorological data sets at a degraded resolution ( $2^\circ$  latitude by  $2.5^\circ$  longitude). All standard and  
16 perturbation full-chemistry simulations for July-August as presented in this paper were conducted  
17 with a 6-month spinup.

18 The different convective parameterizations used to generate the meteorological data sets  
19 alters the characteristics of convective transport of chemical species. Both fvGCM and GEOS4  
20 use the deep convection scheme of Zhang and McFarlane (1995) and the shallow convection  
21 scheme of Hack (1994) whereas MERRA uses a modified version of the Relaxed Arakawa-  
22 Schubert scheme for convection (Moorthi and Suarez, 1992). Figure 1 shows the latitude-pressure  
23 cross sections of zonal mean convective mass fluxes averaged over three meteorological data fields

Deleted: )

1 and the differences from the average during July – August. fvGCM shows the strongest shallow  
2 convection in the Southern Hemisphere (SH) mid- and low-latitudes among the models. GEOS4  
3 shows the strongest convection in the tropical middle troposphere. MERRA is characterized by  
4 the weakest shallow convection in both hemispheres. MERRA has the strongest tropical  
5 convection in the lower free troposphere, but its tropical convection is not as deep as in the others.  
6 Shallow convection in fvGCM and GEOS4 extends to higher latitudes compared to MERRA.

### 7 **2.1.3. Radionuclide Tracers**

8 We conduct GMI model simulations of radionuclides ( $^{222}\text{Rn}$ ,  $^{210}\text{Pb}$ , and  $^7\text{Be}$ ) to examine  
9 the relative effects of convection, stratospheric influence, and large-scale subsidence on the  
10 transport of trace species and their sensitivity to input meteorological data sets.  $^{222}\text{Rn}$  has a half-  
11 life of 3.8 days and is emitted primarily from continental crust. It is useful as a tracer of convective  
12 transport in global models (e.g., Jacob et al., 1997).  $^{210}\text{Pb}$ , a decay daughter of  $^{222}\text{Rn}$ , has a  
13 radioactive half-life of 22.3 years, and  $^7\text{Be}$ , which is produced by cosmic ray spallation reactions  
14 in the stratosphere and UT, has a radioactive half-life of 53.3 days. Because  $^{210}\text{Pb}$  and  $^7\text{Be}$  attach  
15 to submicron aerosols after production and are therefore scavenged by precipitation or deposited  
16 to the surface, they have been used as a pair to test wet deposition schemes in global models (e.g.,  
17 Liu et al., 2001).  $^7\text{Be}$  is also used as a tracer for STE (Dibb et al., 1994; Liu et al., 2001; Liu et al.,  
18 2016). The ratio  $^7\text{Be}/^{210}\text{Pb}$  is useful as an indicator of vertical transport because the ratio is  
19 insensitive to precipitation scavenging (Koch et al., 1996). All simulations of radionuclide tracers  
20 were conducted with a 5-year spinup in order for  $^{210}\text{Pb}$  to reach an equilibrium in the stratosphere.

Formatted: Superscript

## 21 **2.2. Data Sets**

### 22 **2.2.1. Ozonesonde $\text{O}_3$**

1 We use climatological ozone profiles from 23 ozonesonde stations averaged over July –  
2 August from 1985 to 2000, originally constructed by Considine et al. (2008) based on Logan (1999)  
3 and Thompson et al. (2003). The number of soundings at each station is adequate for defining  
4 monthly means used to evaluate the accuracy of the model results (Considine et al., 2008; Liu et  
5 al., 2016).

### 6 **2.2.2. Satellite Tropospheric Ozone Column (TOC)**

7 Three TOC products are used in this study: Total Ozone Mapping Spectrometer (TOMS)  
8 – Solar Backscatter Ultraviolet (SBUV), OMI-MLS, and directly retrieved TOC from TES. The  
9 TOMS-SBUV TOC and OMI-MLS TOC are determined using the tropospheric ozone residual  
10 (TOR) method, which involves subtracting measurements of SBUV and MLS stratospheric  
11 column ozone (SCO) from TOMS and OMI total column ozone, respectively (Fishman et al., 2003;  
12 Ziemke et al., 2006). The TES TOCs are integrated from directly retrieved volume mixing ratios.  
13 We did not consider different instrument sensitivities because integrating retrievals significantly  
14 reduces the error due to averaging over pressure ranges larger than TES vertical resolution  
15 (Osterman et al., 2008; Zhang et al., 2012). The tropopause pressure is taken from the GEOS4  
16 meteorological data ( $2^\circ \times 2.5^\circ$ ). A description of TES retrievals is given in Section 2.2.3.

Deleted: Tropopause

### 17 **2.2.3. TES O<sub>3</sub> and CO.**

18 The TES instrument on EOS-Aura routinely provides observations of tropospheric O<sub>3</sub> and  
19 CO across the globe (Beer et al., 2001; Beer, 2006). The Aura satellite is on a polar sun-  
20 synchronous orbit with equator crossing at 01:45 (descending) and 13:45 (ascending) local time.  
21 TES is a Fourier transform infrared emission spectrometer with high spectral resolution ( $0.1 \text{ cm}^{-1}$ )  
22 and wide spectral range ( $650 - 3050 \text{ cm}^{-1}$ ) (Beer et al., 2001). The nadir footprint of TES is  $5 \times 8$

1 km. TES observations consist of two modes: global survey and special observations (Beer et al.,  
2 2001). We use TES level 2, version 4 global survey nadir observations  
3 (<http://eosweb.larc.nasa.gov/>) and only O<sub>3</sub> and CO retrievals with the “Master” quality flag are  
4 used in this analysis. The retrievals of O<sub>3</sub> have 1 – 1.5 degrees of freedom (DOF) in the profile at  
5 mid-latitudes in summer, with peak sensitivities near 700 hPa and 300-400 hPa, respectively  
6 (Parrington et al., 2008). TES CO profiles generally have 1 – 1.5 DOFs in the troposphere (Luo et  
7 al., 2007ab). Detailed descriptions of the TES instrument and the O<sub>3</sub> and CO retrieval algorithms  
8 are described in Beer et al. (2001, 2006), Worden et al. (2004), and Bowman et al. (2002, 2006).

9 In this study, we use O<sub>3</sub> and CO retrievals at 618 hPa level, where TES has good sensitivity  
10 for both O<sub>3</sub> and CO centered in the MT, and exclude latitudes > 60° where TES measurements are  
11 less reliable due to low brightness temperatures (Zhang et al., 2006). Due to limitation of TES  
12 vertical resolution (1 – 1.5 DOFs in the troposphere for both O<sub>3</sub> and CO), TES averaging kernels  
13 are applied to the simulations to take into account the different sensitivities of the instruments.  
14 TES uses MOZART model output binned by month and in blocks of 10° latitude by 60° longitude  
15 as a priori profiles (Worden et al., 2004). Validation of TES O<sub>3</sub> against ozonesondes showed that  
16 TES ozone typically has a high bias of about 10% in the UT (Worden et al., 2007) or 3-10 ppbv in  
17 the MT/UT (Nassar et al., 2008). TES CO has a negative bias (<10%) compared to aircraft  
18 measurements in the NH mid-latitude LT/MT during the INTEX-B mission (spring 2006) (Luo et  
19 al., 2007a).

20

### 21 **3. Model Simulations of Radionuclides, O<sub>3</sub>, and CO**

#### 22 **3.1. GMI Simulations of Radionuclides**

1            Figures 2 and 3 show the latitude-pressure cross sections of zonal mean concentrations of  
2  $^{222}\text{Rn}$  and stratospheric fraction (%) of tropospheric  $^7\text{Be}$  concentrations during July – August for  
3 the values averaged over three meteorological data sets and the differences from the mean.  
4 Differences in zonal mean  $^{222}\text{Rn}$  concentrations at SH mid-latitudes among the three simulations  
5 are small despite much stronger shallow convection in fvGCM (Figure 1). This reflects the fact  
6 that most convection at SH mid-latitudes occurs over the ocean. However, GMI/fvGCM  $^{222}\text{Rn}$   
7 concentrations in the UT at NH subtropics and mid-latitudes are ~ 20 – 70 % higher than those in  
8 other simulations due to the deeper convection in fvGCM (Figure 1). In the tropical UT/MT,  
9 GMI/MERRA produced the lowest  $^{222}\text{Rn}$  concentrations, consistent with the lower cutoff of  
10 convection in GMI/MERRA (Figure 2). This is not inconsistent with the largest stratospheric  
11 influence in the tropical UT/MT in GMI/MERRA among the three meteorological data sets (Figure  
12 3). Previously, Liu et al. (2010) and Zhang et al. (2011) used GEOS-Chem simulations of CO and  
13  $^{222}\text{Rn}$  (driven by GEOS4 DAS and GEOS5 DAS meteorological data) to show that the tropical  
14 convection in GEOS4 is deeper than in GEOS5. Because the MERRA reanalysis utilizes the same  
15 GCM as the GEOS5 DAS, it also utilizes the Relaxed Arakawa-Schubert (RAS) convection.

16            The stratospheric contribution to the lower-tropospheric  $^7\text{Be}$  concentrations in  
17 GMI/fvGCM peaks near 30 - 75°N (20 – 25%), in contrast to the GMI/GEOS4 and GMI/MERRA  
18 simulations (Figure 3). The GMI/GEOS4 and GMI/MERRA simulations show a similar pattern of  
19 stratospheric influence on the troposphere with maxima near 0 – 30°S and >30°S (20 - 30%),  
20 respectively, in the LT. However, GMI/GEOS4 suggests more stratospheric influence than  
21 GMI/MERRA in the MT near 30°S (30 - 35%) and near 30 – 45°N (~ 25%). The stratospheric  
22 impacts on the tropical MT/UT are weakest in GMI/fvGCM and strongest in GMI/MERRA. At  
23 NH mid-latitudes, stratospheric influences on the LT are largest and most extensive in

1 GMI/fvGCM and smallest in GMI/MERRA. These differences in stratospheric influence that  
2 characterize these meteorological data sets will be used to interpret GMI O<sub>3</sub> and CO simulations  
3 driven by these meteorological fields (Sections 3.2 and 4).

### 4 **3.2. GMI Simulations of O<sub>3</sub> and CO**

5 Figures 4-5 show the latitude-pressure cross sections of zonal mean mixing ratios of O<sub>3</sub>  
6 and CO during July – August averaged over three simulations and the differences from the mean.  
7 The latitudinal distributions of O<sub>3</sub> from all simulations show lowest O<sub>3</sub> concentrations near the  
8 surface at high latitudes and in the tropical LT (Figure 4). Relatively low O<sub>3</sub> in the tropical free  
9 troposphere results from transport of ozone-poor air from the LT to UT/MT via deep convection.  
10 High O<sub>3</sub> concentrations are seen in the (subtropical) descending branches of the Hadley circulation  
11 partly due to the influence of STE. Compared with GMI GEOS4 and GMI/MERRA, GMI/fvGCM  
12 simulates higher O<sub>3</sub> in the NH mid-latitude MT and lower O<sub>3</sub> in the SH LT/MT. This is likely due  
13 to higher STE in the NH and weaker STE in the SH, respectively, as suggested by the higher (lower)  
14 fraction of stratospheric <sup>7</sup>Be seen in the GMI/fvGCM simulation compared to the other two  
15 simulations (Figure 3). On the other hand, GMI/MERRA simulates the highest O<sub>3</sub> in the tropical  
16 MT/UT as a result of “stronger but shallower” deep convection in the tropics (Figure 1). All  
17 simulations show the largest CO concentrations in the tropical LT/MT and NH mid-latitude  
18 boundary layer (Figure 5). The former reflects convective lifting of tropical biomass burning CO  
19 emissions and the latter anthropogenic CO emissions, respectively. Among the three simulations,  
20 GMI/fvGCM simulates the lowest CO concentrations in the tropical MT/UT as well as both  
21 hemispheres. In the NH MT/UT in GMI/fvGCM, the low CO concentrations result from high OH  
22 concentrations associated with high O<sub>3</sub> concentrations due to higher STE, which will be discussed  
23 in Section 4.1. In the SH GMI/fvGCM, the low CO concentrations are due to high OH

1 concentrations as a result of too low  $\text{NO}_x$  emissions from lightning (see Section 4.1). Tropical  
2 MT/UT CO concentrations in GMI/MERRA are not as high as those in GMI/GEOS4, again  
3 reflecting the “shallower” tropical deep convection in MERRA.

4

#### 5 **4. Evaluation of GMI $\text{O}_3$ and CO Simulations with Observations**

6 In this section, we evaluate GMI  $\text{O}_3$  and CO simulations driven by the fvGCM, GEOS4,  
7 and MERRA meteorological data sets with ozonesonde  $\text{O}_3$  vertical profiles, satellite TOC, and  
8 TES  $\text{O}_3$  and CO retrievals.

#### 9 **4.1. Ozone Vertical Profiles and Tropospheric Ozone Column**

10 Figure 6 compares GMI simulated tropospheric  $\text{O}_3$  profiles with ozonesonde observations  
11 averaged over July-August for a range of latitudes. These results are typical of other stations at  
12 similar latitudes. The mean differences between simulated  $\text{O}_3$  and ozonesonde observations at 500  
13 hPa (MT) and 200 hPa (UT), respectively, are listed in Table 2. GMI/fvGCM overestimates  $\text{O}_3$  in  
14 the NH high-/mid-latitude UT/MT (e.g., Churchill, Hohenpeissenberg, and Sapporo). This may be  
15 due to excessive STE given the relatively high fractions of  $^7\text{Be}$  from the stratosphere (Figure 3).  
16 The overestimate may also be partly attributed to strong convective mass fluxes in the NH mid-  
17 latitude that lift more  $\text{O}_3$  and/or its precursors from the surface (Figures 1-2). Figure 6 also shows  
18 that GMI/fvGCM underestimates  $\text{O}_3$  in the SH (e.g., Reunion Island). Since stratospheric  $^7\text{Be}$   
19 fractions are relatively low in this simulation, the  $\text{O}_3$  underestimate may be due to overly weak  
20 STE (cf. Figure 3). Low emissions of lightning  $\text{NO}_x$ , an important precursor of tropospheric  $\text{O}_3$   
21 could also play a role. It is noted that all simulations show hot spots of  $\text{LNO}_x$  emissions over the central  
22 and eastern US, central Africa, and west Tibetan plateau (not shown). Lightning  $\text{NO}_x$  emissions between

Formatted: Subscript

Deleted: representing MT and UT,

Formatted: Subscript

1 10°S and 70°S in GMI/fvGCM during July-August are similar to those in GMI/GEOS4 and  
2 GMI/MERRA, but the emissions during May-June are a factor of ~ 2.5 lower than those in  
3 GMI/GEOS4 and GMI/MERRA (Table 1). Since O<sub>3</sub> has a lifetime of weeks to months in the  
4 UT/MT, a low-O<sub>3</sub> bias during May-June will lead to lower O<sub>3</sub> during July-August in GMI/fvGCM.  
5 GMI/GEOS4 simulates O<sub>3</sub> in both hemispheres reasonably well but underestimates O<sub>3</sub> in the  
6 tropical UT/MT, as seen at Paramaribo and Nairobi in Figure 6. GMI/MERRA underestimates O<sub>3</sub>  
7 in the NH high-latitude UT (e.g., Resolute) likely due to weak STE compared to GMI/GEOS4 as  
8 suggested by <sup>7</sup>Be tracer simulations (Figure 3), while it overestimates O<sub>3</sub> with a high bias in the  
9 SH subtropics (e.g., Samoa and Reunion Island) because of a combination of excessive influences  
10 from lightning NO<sub>x</sub> emissions in May (Table 1) and STE (or subsidence from UT) (Figure 3). In  
11 addition, the shallower tropical convection (Figure 1) accompanied by larger STE contribution in  
12 the southern tropical MT/UT (Figure 3) results in less clean air being lifted from the LT to MT/UT.

13 Figure 7 shows GMI simulated zonal mean TOCs averaged over July – August in  
14 comparison with TORs determined from TOMS/SBUV (Fishman et al., 2003), OMI/MLS  
15 (Ziemke et al., 2006), and TOCs directly retrieved from TES measurements. The World  
16 Meteorological Organization (WMO) definition of thermal tropopause is used to calculate the  
17 model TOC, following Liu et al. (2016). The latitudinal distribution of TOCs shows a trough in  
18 the tropics and polar regions, and a peak at mid-latitudes in both the models and the observations.  
19 The TORs determined from TOMS/SBUV and OMI/MLS agree well with each other in the NH,  
20 but those from OMI/MLS are lower at ~10°N and higher at south of 50°S. The TOCs determined  
21 from TES are more similar to the OMI/MLS TORs, but biased high in the northern subtropics, and  
22 biased low at south of 40°S. A comparison of Figure 7 with Figure 6 indicates that the TOCs from  
23 three model simulations coincide with the above results from model evaluations with ozonesonde

1 O<sub>3</sub> profiles. For example, both evaluations suggest negative biases in the SH and positive biases  
2 in the NH high-/mid-latitudes in GMI/fvGCM, and positive biases in the southern subtropics in  
3 GMI/MERRA.

#### 4 **4.2. O<sub>3</sub> and CO Concentrations at 618 hPa**

5 Figure 8 shows the July-August mean concentrations of O<sub>3</sub> and CO at 618 hPa in the GMI  
6 simulations. Figure 9 shows the corresponding global distributions of <sup>222</sup>Rn concentrations,  
7 stratospheric fractions (%) of mean tropospheric <sup>7</sup>Be concentrations, and ratios <sup>7</sup>Be/<sup>210</sup>Pb. All  
8 simulations show highest O<sub>3</sub> concentrations at NH mid-latitudes and lowest O<sub>3</sub> concentrations in  
9 the tropical western Pacific. They also simulate a narrow band of relatively high O<sub>3</sub> concentrations  
10 in the southern tropics and subtropics. GMI/fvGCM simulates highest O<sub>3</sub> concentrations at NH  
11 mid/high latitudes (Figure 8, left panel) likely due to STE, as indicated by a large fraction of <sup>7</sup>Be  
12 transported down from the stratosphere (Figure 9, middle top panel). By contrast, it simulates the  
13 lowest O<sub>3</sub> concentrations in the southern tropics and subtropics, especially over southern Africa  
14 and South Atlantic Ocean. In this region, GMI/MERRA simulates the highest O<sub>3</sub> concentrations  
15 attributed to high lightning NO<sub>x</sub> emissions (Table 1), large STE (Figure 9, middle bottom panel),  
16 and biomass burning emissions lifted by shallow but strong convection (Section 3; Figure 9, left  
17 bottom panel). Thompson et al. (1996) previously suggested that the O<sub>3</sub> maximum observed in  
18 southern Africa and the adjacent Atlantic during September - October 1992 is caused by the  
19 coincidence of O<sub>3</sub> precursors from biomass burning with long residence time, and deep convection  
20 with additional lightning NO<sub>x</sub> and biogenic sources. As we will show in Section 5, the emission  
21 types contributing to the O<sub>3</sub> enhancements over this region in July – August mainly include  
22 lightning NO<sub>x</sub> and, to a lesser extent, biomass burning.

1 All simulations show a similar pattern of CO concentrations at 618 hPa, e.g., CO  
2 enhancements due to biomass burning emissions lifted by convection (e.g., South America, Africa,  
3 Indonesia, and Alaska) and anthropogenic emissions (e.g., East Asia, South Asia, and eastern  
4 North America) (Figure 8, right column). This pattern also reflects the geographic distribution of  
5 these emissions. GMI/fvGCM simulates lowest CO concentrations at 618 hPa in most of the  
6 polluted regions due to stronger STE of O<sub>3</sub>, as discussed in Section 4.1. GMI/GEOS4 simulates  
7 slightly lower CO concentrations in East and South Asia, North America and their outflow regions,  
8 and Indonesia than GMI/MERRA does. GMI/GEOS4 also simulates lower CO concentrations over  
9 subtropical South American and African westerly outflow regions.

10 To evaluate GMI O<sub>3</sub> and CO simulations with satellite observations, we use TES retrievals  
11 at 618 hPa where TES has good sensitivity for both O<sub>3</sub> and CO in the MT (Zhang et al., 2006).  
12 GMI model output was sampled along the TES orbit track at the observation time and then  
13 interpolated onto the 67 vertical pressure levels of TES retrievals. Since the model output was  
14 saved every 3 hours, the temporal offset with TES is up to 1.5 hours. To compare the model output  
15 with the TES retrieved profiles, TES averaging kernels and *a priori* were applied to the model  
16 output. Both the model output and TES data were gridded onto grids of 10° latitude by 10°  
17 longitude by averaging all values within each grid box. Figures 10-11 show the mean  
18 concentrations of O<sub>3</sub> and CO at 618 hPa observed by TES during July - August 2005 and  
19 corresponding GMI CTM results.

20 TES observed enhanced O<sub>3</sub> concentrations over the Middle East, northern Africa, southern  
21 Africa, North America, and East Asia (Figure 10). Increased levels of O<sub>3</sub> were also observed in  
22 continental outflow regions, especially the northwestern Pacific, North Atlantic, tropical south  
23 Atlantic, and southern subtropical Indian Ocean. All simulations capture the spatial distributions

1 of O<sub>3</sub> well but underestimate the enhancements over southern Africa and adjacent oceans.  
2 GMI/fvGCM simulates reasonably well the TES-observed O<sub>3</sub> enhancements at NH mid/high  
3 latitudes but slightly underestimates the low O<sub>3</sub> concentrations in the tropical western Pacific and  
4 Indian Ocean. GMI/GEOS4 and GMI/MERRA simulations show lower O<sub>3</sub> concentrations at NH  
5 mid/high latitudes compared to TES observations. However, considering that TES O<sub>3</sub> has a  
6 positive bias of 3-10 ppbv in the MT (Nassar et al., 2008), GMI/fvGCM may very well  
7 overestimate O<sub>3</sub> at NH mid-latitudes while GMI/GEOS4 and GMI/MERRA simulations are closer  
8 to reality. This conclusion is consistent with that from the comparison of GMI simulations with  
9 ozonesonde observations (Figure 6).

10 Enhanced CO concentrations were observed by TES over Africa, South America, North  
11 America, and Eurasia (Figure 11). All simulations underestimated CO concentrations in most of  
12 those CO hot spots in the NH. GMI/GEOS4 captured fairly well high CO concentrations over  
13 biomass burning regions in South America and Africa. However, considering TES CO biases, i.e.,  
14 a negative bias at NH mid-latitudes and a positive bias in the tropics (Luo et al., 2007a; Lopez et  
15 al., 2008), all simulations significantly underestimate CO enhancements at NH mid-latitudes but  
16 simulate better CO enhancements over the tropical biomass burning regions. This is consistent  
17 with a previous study by Shindell et al. (2006) who found a multi-model underestimate of NH  
18 extratropical CO likely due to current inventories underestimating fossil fuel emissions in East  
19 Asia and biomass burning emissions in south-central Africa.

20

## 21 5. O<sub>3</sub> and CO Relationships

1 In this section, we examine O<sub>3</sub> and CO relationships at 618hPa in GMI CTM. We interpret  
2 GMI simulated O<sub>3</sub>-CO correlations and their slopes in the context of emissions, photochemical  
3 transformation, and transport (e.g., convection, STE, and large-scale subsidence), using model  
4 meteorological data and radionuclide simulations. We then evaluate them with those derived from  
5 TES satellite observations. Note that the model underestimate of CO concentrations does not significantly  
6 affect the calculated O<sub>3</sub>-CO correlations although it may cause biases in the regression slopes due to the  
7 association of the latter with ozone production efficiency.

### 8 **5.1. GMI O<sub>3</sub>-CO Correlations**

9 Figure 12 shows the O<sub>3</sub>-CO correlation coefficients (R) and linear regression slopes  
10 (dO<sub>3</sub>/dCO) at 618 hPa for July – August, as calculated using the reduced major axis method with  
11 3-hourly output from the GMI/fvGCM, GMI/GEOS4, and GMI/MERRA simulations. We discuss  
12 the common features in the correlation patterns in all simulations, followed by their discrepancies.  
13 All simulations show strong positive O<sub>3</sub>-CO correlations and large dO<sub>3</sub>/dCO enhancement ratios  
14 in the NH major continental outflow regions, e.g., Atlantic Seaboard, northern Atlantic, and  
15 northern Pacific, consistent with previous modeling studies (Zhang et al., 2006; Voulgarakis et al.,  
16 2011) and in situ observations (e.g., Anderson et al. 1993; Chin et al., 1994; Jaffe et al., 1996;  
17 Parrish et al., 1998; Tsutsumi and Matsueda, 2000; Mao and Talbot, 2004). Our simulations also  
18 suggest a much larger area with high correlations that extends from the NW to NE Pacific. We  
19 found that strong positive correlation regions are not co-located with maximum O<sub>3</sub> and CO  
20 concentrations in all simulations. Instead, they are located between most polluted and clean areas,  
21 reflecting the intrusion of high O<sub>3</sub> (and CO) air from mid-latitudes and low O<sub>3</sub> (and CO) air from  
22 the tropics. Fishman and Seiler (1983) and Mauzerall et al. (2000) previously suggested that strong

1 positive O<sub>3</sub>-CO correlations in low CO regions may be caused by the depletion of both O<sub>3</sub> and CO  
2 in tropical air.

3 All simulations show positive O<sub>3</sub>-CO correlations in the SH marine regions, but  
4 GMI/MERRA simulates much stronger negative correlations over the equatorial Atlantic. The  
5 latter reflects the stronger convection in the LT/MT in MERRA, which will be discussed below.  
6 Positive O<sub>3</sub>-CO correlations were previously observed over the tropical South Atlantic during the  
7 TRACE-A aircraft mission (September–October, 1992) (e.g., Collins et al., 1996). Collins et al.  
8 concluded that the O<sub>3</sub>-CO correlations over the tropical South Atlantic are more affected by in situ  
9 photochemical production from aged biomass burning plumes (positive O<sub>3</sub>-CO correlation) than  
10 transport from the stratosphere (negative O<sub>3</sub>-CO and O<sub>3</sub> - dew point correlations).

11 Strong positive O<sub>3</sub>-CO correlations are present in all simulations at 618 hPa over [western](#)  
12 [and central](#) Indonesia (Figure 12), reflecting convective transport of biomass burning CO (Figure  
13 8) and photochemical production of O<sub>3</sub> from its precursors. The dO<sub>3</sub>/dCO enhancement ratios over  
14 Indonesia are not as large as those over the NH mid-latitude continental outflow regions due to the  
15 fact that biomass burning emits NO<sub>x</sub> less efficiently than fossil fuel does.

16 Positive O<sub>3</sub>-CO correlations over the westerly African biomass burning outflow region  
17 (southern Indian Ocean, ~ 45°S) are seen in all simulations (Figure 12). The positive O<sub>3</sub>-CO  
18 correlations over both the NH mid-latitude continental outflow regions and the westerly African  
19 biomass burning outflow regions mainly reflect O<sub>3</sub> and CO signatures from different sources: 1)  
20 anthropogenic emissions of CO and other O<sub>3</sub> precursors in the former and biomass burning  
21 emissions in the latter (Figure 8), and 2) significant influences from the stratosphere and  
22 subsidence from UT/LS (Figure 9, middle and right columns, respectively). In the case of 1), the

Deleted: /

1  $dO_3/dCO$  slopes in the westerly African biomass burning outflow are smaller than those in the NH  
2 mid-latitude continental outflow, again reflecting the lower efficiency of biomass burning  $NO_x$   
3 emissions than that of fossil fuel  $NO_x$  emissions. In the case of 2), mixing of stratospheric air (high  
4  $O_3$ ) with polluted air masses (high CO) has previously been found associated with positive  $O_3$ -CO  
5 correlations downwind from outflow regions (Cooper et al., 2002; Kim et al., 2013).

6 Strong negative  $O_3$ -CO correlations are seen in all simulations over the northern tropical  
7 eastern Pacific, Caribbean, northern tropical Atlantic, and equatorial Africa. These negative  
8 correlations are primarily a result of convective transport of low- $O_3$  air masses impacted by  
9 biogenic emissions. As will be discussed in Section 6, significant decreases in  $O_3$  and increases in  
10 CO occur near the above regions due to atmospheric oxidation of biogenic VOCs (e.g., isoprene)  
11 over tropical America and Africa. In addition, our results show weak positive (in GMI/fvGCM  
12 and GMI/GEOS4) or strong negative (in GMI/MERRA)  $O_3$ -CO correlations over much of the  
13 southern tropics and subtropics, especially near the biomass burning outflow regions. Negative  
14  $O_3$ -CO correlations in the southern tropics during July-August were previously reported by  
15 Fishman and Seiler (1983). Based on aircraft measurements, they concluded that  $O_3$  destruction in  
16 the southern tropical LT, where the major CO sources (biomass burning emissions) are located,  
17 may lead to strong negative correlations (see their Figure 3).

18 All GMI simulations show strong negative  $O_3$ -CO correlations over the Asian continent  
19 including the Middle East (Figure 12). Over Southwest China (e.g., Sichuan Basin), monsoonal  
20 convective lifting of air masses with high-CO and low- $O_3$  leads to negative  $O_3$ -CO correlations.  
21 For most of other regions, high  $O_3$  and low CO associated with stratospherically influenced air  
22 (Figure 9, middle column) result in negative  $O_3$ -CO correlations with large (negative)  $dO_3/dCO$   
23 ratios. As will be discussed in Section 6, lightning  $NO_x$  emissions also contribute to these negative

1 correlations over the Asian continent. Our simulations over the Tibetan Plateau are consistent with  
2 the study of Wang et al., (2006), who inferred negative O<sub>3</sub>-CO correlations from in situ  
3 measurements at Mount Waliguan located at the northeastern edge of the Tibetan Plateau during  
4 summer due to downward transport from the UT/LS.

5 While the O<sub>3</sub>-CO correlations in the three simulations show similarities, they also show  
6 differences. The global O<sub>3</sub>-CO correlation patterns in GMI/fvGCM and GMI/GEOS4 are more  
7 similar, presumably because fvGCM is the GCM in the GEOS4 assimilation and they use the same  
8 convection scheme. Even so, significantly different O<sub>3</sub>-CO correlation coefficients between  
9 GMI/fvGCM and GMI/GEOS4 are seen in northern Africa, where the former simulates strong  
10 negative but the latter shows weak positive correlations. As indicated by radionuclide tracers (<sup>210</sup>Pb  
11 and <sup>7</sup>Be), fvGCM has relatively stronger large-scale subsidence over northern Africa at 618 hPa  
12 than GEOS4, resulting in strong correlations with a large negative slope. In addition, the O<sub>3</sub>-CO  
13 correlations in GMI/MERRA are strongly negative over northern South America, tropical western  
14 South Atlantic Ocean, Indian Ocean, and tropical western Pacific Ocean. By contrast, the  
15 correlations in these regions in GMI/fvGCM and GMI/GEOS4 are either weak or positive. The  
16 convection in fvGCM is much weaker than in GEOS4 or MERRA except at SH mid-latitudes and  
17 over Tibetan Plateau (not shown). MERRA has the strongest convection in Central America,  
18 tropical western Pacific Ocean, tropical eastern Pacific Ocean, tropical western Atlantic Ocean,  
19 tropical eastern Indian Ocean, and Bay of Bengal. These differences of convective mass fluxes  
20 result in broader regions with negative O<sub>3</sub>-CO correlations in the tropics in GMI/MERRA than  
21 those in GMI/fvGCM and GMI/GEOS4. Kim et al. (2013) also simulated different O<sub>3</sub>-CO  
22 correlations in some tropical regions with GEOS-Chem driven by GEOS4 and GEOS5  
23 meteorological data sets because of the model transport error associated with deep convection.

## 1 5.2. Evaluation of GMI O<sub>3</sub>-CO Correlations with TES Observations

2 Figures 13 and 14 show the O<sub>3</sub>-CO correlation coefficients (R) and linear regression slopes  
3 (dO<sub>3</sub>/dCO), respectively, at 618 hPa as determined by TES observations for July - August 2005,  
4 and corresponding GMI CTM results with 3-hourly output sampled along the TES orbit tracks.  
5 Values are calculated in 10°x10° grid cells. The regions of > 60°S and > 60°N are excluded in this  
6 study because O<sub>3</sub> and CO concentrations over these regions are low (Figure 8) and absolute co-  
7 variances of O<sub>3</sub> and CO over these regions are also low (not shown). Therefore, as suggested by  
8 Voulgarakis et al. (2011), discrepancies in these regions are not scientifically important in terms  
9 of the O<sub>3</sub>-CO correlation. Since only two months of TES O<sub>3</sub> and CO observations were used, the  
10 correlation patterns are somewhat patchy and correlations are weak ( $|R| < 0.2$ ) over more than half  
11 of the globe. Using TES data for July – August over 5 years improves the consistency of the  
12 correlation patterns (Figure 15), as discussed later. TES-observed O<sub>3</sub> and CO concentrations show  
13 highest correlations (R up to 0.6) with large slopes over the western Pacific, and relatively high  
14 correlations (R = 0.2-0.4) with relatively large slopes over North America, the Middle East,  
15 northern South America, central and southern Africa, as well as continental outflow regions, e.g.,  
16 northwestern Pacific Ocean, western Indian Ocean, subtropical South Atlantic Ocean, tropical  
17 eastern Pacific, and northwestern Atlantic (Figures 13 and 14). Negative correlations were  
18 observed over the Tibetan Plateau (R < -0.6), northern Africa, and SH mid-latitudes (R < -0.4)  
19 (Figure 13). Global TES O<sub>3</sub>-CO correlation patterns and magnitudes are similar to those reported  
20 by Zhang et al. (2006) and Voulgarakis et al. (2011). The slope patterns (Figure 14) follow the  
21 correlation ones (Figure 13), suggesting that the slopes of the regression lines are useful indicators  
22 of the correlation strength.

1           The GMI simulated O<sub>3</sub>-CO correlation coefficients and linear regression slopes (dO<sub>3</sub>/dCO)  
2 calculated from each of the three model outputs sampled along the TES orbit tracks show similar  
3 global patterns but overall weaker correlations (Figure 13) and smaller slopes (Figure 14) than  
4 non-sampled raw model results (Figure 12) due to spatiotemporal sampling and application of TES  
5 averaging kernels. All simulations capture the TES-observed positive O<sub>3</sub>-CO correlations in  
6 various regions. On the other hand, all simulations indicate strong negative correlations over the  
7 Tibetan Plateau and tropical convective regions where TES misses such correlations or only shows  
8 much weaker negative correlations in much narrower areas.

9           To get a more statistically robust view of TES O<sub>3</sub>-CO correlations, we conduct a similar  
10 analysis using multi-year observations. Figure 15 shows the O<sub>3</sub>-CO correlation coefficients (R)  
11 and linear regression slopes (dO<sub>3</sub>/dCO) at 618 hPa as determined by TES O<sub>3</sub> and CO retrievals for  
12 July - August over 5 years (2005 – 2009). Values are calculated in 4°x5° grid cells. The global  
13 distributions provide more details and are consistent with the coarse patterns for July – August  
14 2005 shown in Figures 13 and 14. The negative correlations over the Tibetan Plateau and northern  
15 Africa are more apparent than those using the TES data only for July – August 2005 (Figure 13).  
16 Overall our results of multi-year (2005 – 2009) O<sub>3</sub>-CO correlation coefficients at 618 hPa for July  
17 – August are similar to those inferred from the mean mid-tropospheric (400 – 800 hPa) TES O<sub>3</sub>  
18 and CO concentrations averaged over July – August 2005 – 2008 (Voulgarakis et al., 2011).

19

## 20 **6. Sensitivity of O<sub>3</sub>-CO Correlations to Emissions**

21           In order to understand how O<sub>3</sub>-CO correlation patterns are driven by emissions, we  
22 examine the sensitivity of O<sub>3</sub>-CO correlations to emission types in the GMI model driven by the

1 MERRA meteorological fields, which represent the state-of-the-art of GEOS-DAS at the time of  
2 this study. Figures 16 - 19 show the mean changes in O<sub>3</sub> and CO concentrations (ppbv) and their  
3 correlation coefficients, as well as the areas where correlation signs change relative to the standard  
4 simulation at 618 hPa when each emission type (fossil fuel, biomass burning, biogenic, and  
5 lightning NO<sub>x</sub> emissions) is excluded in the model for July – August 2005. Figure 20 shows the  
6 O<sub>3</sub>-CO correlation coefficients (R) at 618 hPa in the standard simulation and when each emission  
7 type is excluded. Results are calculated using 3-hourly model output. These figures provide the  
8 context for discussions in this section.

9 Fossil fuel emissions substantially increase O<sub>3</sub> (by ~5-20 ppbv) and CO (by ~10-30 ppbv)  
10 in the NH, notably over the Asian and North American continental outflow regions (Figure 16ab).  
11 Fossil fuel emissions lead to strengthened O<sub>3</sub>-CO correlations with correlation signs changing from  
12 negative to positive over the Asian and North American outflow regions (Figures 16cd and 20b).  
13 Such effects are also seen over Europe, the Arabian Sea, the northern Bay of Bengal, and the  
14 northeastern Pacific (Figure 16cd). Fossil fuel emissions result in stronger negative O<sub>3</sub>-CO  
15 correlations over part of the Asian continent (Figure 16c). This is especially true over the Tibetan  
16 Plateau where low-level convergence transports air masses with low-O<sub>3</sub> and high-CO to the middle  
17 troposphere.

18 Biomass burning emissions increase O<sub>3</sub> (by ~2-10 ppbv) and CO (by > 25ppbv) in the  
19 easterly outflow in the tropical South America and Central Africa, in the westerly outflow in the  
20 southern subtropics, and over Indonesia (Figure 17ab). They are responsible for the positive  
21 correlations in the SH mid- and high- latitudes (Figures 17cd and 19c). Without biomass burning  
22 emissions, O<sub>3</sub>-CO correlations over the westerly outflow in the southern subtropics and most of  
23 the SH mid- and high- latitudes would be negative or very weak (Figures 17c and 20c). By contrast,

1 biomass burning emissions degrade an already strong correlation from fossil fuel emissions in the  
2 NH (e.g., over part of the tropical western Pacific, Bay of Bengal, NH subtropical Atlantic, and  
3 especially NH high latitudes, Figure 17d). In the tropics, biomass burning emissions strengthen  
4 the positive correlations in Indonesia and weaken the negative correlations over the tropical South  
5 American outflow region. In the two models of Voulgarakis et al. (2011), biomass burning  
6 emissions have the largest impact on the O<sub>3</sub>-CO correlations in the tropics, especially downwind  
7 of Central Africa and South America where biomass burning emissions changed the correlation  
8 sign from negative to positive. Our results show no apparent changes in the O<sub>3</sub>-CO correlation  
9 signs (negative) in these downwind regions. This may reflect the differences in biomass burning  
10 emissions and/or chemical mechanisms used in the two studies.

11 Biogenic emissions increase O<sub>3</sub> concentrations at 618 hPa by ~ 2-6 ppbv in the NH  
12 subtropics and mid-latitudes, but decrease O<sub>3</sub> concentrations by up to ~10 ppbv in tropical South  
13 America, tropical Africa, and Indonesia (Figure 18a). The latter mainly reflects the fact that O<sub>3</sub> is  
14 consumed during the atmospheric oxidation process of isoprene under low NO<sub>x</sub> conditions (Fan  
15 and Zhang, 2004; Seinfeld and Pandis, 1998). Biogenic emissions have large positive impacts on  
16 CO concentrations in the easterly and westerly outflow regions of South America and Africa, in  
17 the North American outflow, over Southwest China and Indonesia, as well as in the SH background  
18 (Figure 18b). The O<sub>3</sub>-CO correlations in the model show smaller sensitivity to biogenic emissions  
19 relative to other emission types (Figures 18c and 20d). Nevertheless, biogenic emissions lead to  
20 strong negative O<sub>3</sub>-CO correlations over the tropical eastern Pacific Ocean due to reduced O<sub>3</sub> and  
21 enhanced CO concentrations associated with these emissions (Figures 18cd and 20d). Such effects  
22 are also seen over central Africa, easterly South American outflow, westerly South American  
23 outflow, Indonesia, and subtropical western Pacific.

1 Lightning NO<sub>x</sub> emissions increase O<sub>3</sub> concentrations at 618 hPa by up to ~15-25 ppbv at  
2 NH subtropics and mid-latitudes, and by up to ~15-30 ppbv at SH tropics and subtropics (Figure  
3 19a). Such increases are relatively larger in those regions with subsiding air from the UT (cf.,  
4 Figure 9, right bottom panel), where the largest effect of lightning NO<sub>x</sub> emissions occurs. The  
5 resulting increase in OH concentrations leads to a general decrease in CO concentrations with  
6 maximum effects in the tropics and SH subtropics (Figure 19ab). Consequently, lightning NO<sub>x</sub>  
7 emissions weaken both the positive O<sub>3</sub>-CO correlations at mid- and high- latitudes and the negative  
8 correlations in the tropics (Figures 19cd and 20e). They alter the correlation signs from positive to  
9 negative in various areas where the correlations are generally weak (Figure 19d). Our results are  
10 in contrast with those of Voulgarakis et al. (2011) who showed that lightning NO<sub>x</sub> emissions  
11 appeared to increase the O<sub>3</sub>-CO correlations (400-800 hPa) in various regions (e.g., tropical eastern  
12 Pacific, NH continental outflow regions). These may partly reflect the differences in the altitude  
13 and strength of lightning NO<sub>x</sub> emissions.

14

## 15 **7. Summary and Conclusions**

16 We have examined the capability of the Global Modeling Initiative (GMI) chemistry and  
17 transport model (CTM) to reproduce the global mid-tropospheric O<sub>3</sub>-CO correlations from the TES  
18 instrument onboard the NASA Aura satellite during boreal summer (July – August). The model  
19 was driven by three meteorological data sets (fvGCM for 1995, GEOS4 for 2005, MERRA for  
20 2005), allowing us to examine the sensitivity of model O<sub>3</sub>-CO correlations to input meteorological  
21 data. To understand how various emissions drive global O<sub>3</sub>-CO correlation patterns, we also

1 investigated the sensitivity of GMI/MERRA model-calculated O<sub>3</sub> and CO concentrations and their  
2 correlations to emission types.

3 We evaluated GMI-simulated tropospheric O<sub>3</sub> vertical profiles and tropospheric O<sub>3</sub>  
4 columns (TOCs) with those from ozonesonde and satellite observations, respectively. To aid in  
5 the evaluation, model simulations of radionuclide tracers (<sup>222</sup>Rn, <sup>210</sup>Pb, and <sup>7</sup>Be) were used to  
6 illustrate the differences in convection, stratospheric influence, and large-scale subsidence among  
7 three meteorological data sets. Among the three GMI simulations, GMI/GEOS4-simulated O<sub>3</sub>  
8 concentrations are in best agreement with the observations. GMI/MERRA underestimates O<sub>3</sub> in  
9 the NH high-latitude UT due to weak STE, and overestimates O<sub>3</sub> in the SH subtropics. The latter  
10 is due to a combination of excessive influences from lightning NO<sub>x</sub> emissions and STE (or  
11 subsidence), as well as the shallower convection resulting in less low-O<sub>3</sub> air lifted from the LT to  
12 MT/UT. The latitudinal distribution of model biases in TOCs relative to satellite observations is  
13 consistent with the results from model evaluations with ozonesonde O<sub>3</sub> profiles.

14 We evaluated GMI simulated O<sub>3</sub> and CO concentrations with TES observations at 618 hPa  
15 where TES has most sensitivity. TES observed O<sub>3</sub> enhancements over the NH mid-latitudes  
16 (including continental outflow regions), the Middle East, and the subtropical southern Africa and  
17 Atlantic. All simulations well capture the global spatial distribution of O<sub>3</sub> at 618 hPa, but appear  
18 to underestimate TES O<sub>3</sub> observations over southern Africa and its outflow region. GMI/fvGCM  
19 simulates the highest O<sub>3</sub> concentrations at NH mid-/high-latitudes, especially the Asian continent  
20 due to strong STE whereas it simulates the lowest O<sub>3</sub> concentrations in the southern tropics and  
21 subtropics due to weak STE and low lightning NO<sub>x</sub> emissions. GMI/MERRA simulates the highest  
22 O<sub>3</sub> concentrations in the southern subtropics, especially southern Africa due to high lightning NO<sub>x</sub>  
23 emissions and, to a lesser extent, strong convection. GMI/fvGCM underestimates the O<sub>3</sub> minimum

Deleted:

Formatted: Subscript

Formatted: Subscript

Deleted: due to tropical deep convection being too shallow, which results in less low-O<sub>3</sub> air transported from LT to MT/UT, as well as excessive NO<sub>x</sub> emissions from lightning

1 in the tropical western Pacific and eastern Indian Ocean. Considering the positive bias in TES O<sub>3</sub>  
2 at NH mid-latitudes, GMI/fvGCM appears to overestimate O<sub>3</sub> over the East Asian outflow region  
3 due to too fast STE whereas GMI/GEOS4 and GMI/MERRA simulate O<sub>3</sub> enhancements  
4 reasonably well in East Asia and its downwind regions. All three simulations significantly  
5 underestimate TES-observed CO enhancements at NH mid-latitudes, but simulate better CO  
6 enhancements over the tropical biomass burning regions.

7 The three GMI simulations all show strong positive O<sub>3</sub>-CO correlations at 618 hPa over  
8 the NH mid-latitude continental outflow regions and the SH biomass burning outflow regions, as  
9 shown by TES observations. Generally, positive O<sub>3</sub>-CO correlations are simulated downwind of  
10 polluted regions due to photochemical production of O<sub>3</sub> from its precursors. However, owing to  
11 significant influences from the stratosphere and subsidence from UT/LS over these regions, mixing  
12 of stratospheric air with polluted (anthropogenic or biomass burning) air masses is associated with  
13 strong positive O<sub>3</sub>-CO correlations with large dO<sub>3</sub>/dCO enhancement ratios. Strong positive O<sub>3</sub>-  
14 CO correlations are also simulated over the Indonesian biomass burning region where deep  
15 convection occurs, but the dO<sub>3</sub>/dCO enhancement ratios are smaller than those in the NH mid-  
16 latitude continental outflow regions. The latter reflects the lower efficiency of NO<sub>x</sub> emissions from  
17 biomass burning. Strong negative O<sub>3</sub>-CO correlations over northern and central Africa, tropical  
18 Atlantic, and tropical eastern and western Pacific in all simulations result from convective  
19 transport of biomass burning air masses with low-O<sub>3</sub>, and consumption of O<sub>3</sub> along with  
20 production of CO due to oxidation of biogenic hydrocarbons (e.g., isoprene under low NO<sub>x</sub>  
21 conditions). The simulated negative O<sub>3</sub>-CO correlations over the Asian continent, including the  
22 Middle East, are partly attributed to stratospheric influence and/or subsidence from UT/LS. High-  
23 O<sub>3</sub> and low-CO associated with stratospherically influenced air lead to strong negative correlations

Deleted: in

1 with large  $dO_3/dCO$  ratios. On the other hand, over Southwest China, monsoonal convective lifting  
2 of air masses with high-CO and low- $O_3$  results in negative  $O_3$ -CO correlations. By contrast, TES  
3  $O_3$  and CO concentrations at 618 hPa either miss such negative correlations (i.e., tropical  
4 convective regions) or only show weak negative correlations over much narrower areas (i.e., the  
5 Tibetan Plateau and northern Africa).

6 TES-observed  $O_3$  and CO concentrations at 618 hPa show highest positive correlations  
7 with large regression slopes over the western Pacific, and relatively high correlations over North  
8 America, the Middle East, northern South America, central and southern Africa, and continental  
9 outflow regions. Negative correlations are observed in parts of the Asian continent (Tibetan  
10 Plateau), northern Africa, and SH mid-latitudes. All model output sampled along the TES orbit  
11 track capture the observed positive  $O_3$ -CO correlations over the NH mid-latitude continental  
12 outflow regions, southern Africa, western Indian Ocean, subtropical South Atlantic, northern  
13 South America, and tropical eastern Pacific. While all simulations show strong negative  
14 correlations over the Tibetan Plateau, northern Africa, northern subtropical eastern Pacific, and  
15 Caribbean, TES  $O_3$  and CO concentrations at 618 hPa only show weak negative correlations over  
16 much narrower areas (i.e., the Tibetan Plateau and northern Africa).

17 We performed sensitivity simulations with GMI/MERRA to investigate the effect of  
18 individual emission types on model-calculated  $O_3$ -CO correlations at 618 hPa. Results show that  
19 fossil fuel emissions increase global  $O_3$  and CO concentrations and are responsible for the strong  
20 positive correlations over the NH continental outflow regions. Both biomass burning and biogenic  
21 emissions significantly increase global CO concentrations. Biomass burning emissions increase  
22  $O_3$  concentrations in the easterly outflow in the tropical South America and Central Africa, in the  
23 westerly outflow in the southern subtropics, and over Indonesia. Biogenic emissions increase  $O_3$

Deleted:

1 concentrations in the NH subtropics and mid-latitudes, but decrease O<sub>3</sub> concentrations in tropical  
2 South America, tropical Africa, and Indonesia. The decreases mainly reflect the fact that O<sub>3</sub> is  
3 consumed during the atmospheric oxidation process of isoprene under low NO<sub>x</sub> conditions.  
4 Biomass burning emissions are responsible for the positive correlations in the SH mid- and high-  
5 latitudes and negative correlations over part of the tropical western Pacific, Bay of Bengal, NH  
6 subtropical Atlantic, and NH high latitudes. Biogenic emissions have relatively smaller impact on  
7 the correlations than other emissions do, but are largely responsible for the negative O<sub>3</sub>-CO  
8 correlations over the tropical eastern Pacific. Lightning NO<sub>x</sub> emissions lead to large increases in  
9 O<sub>3</sub> concentrations at NH subtropics and mid-latitudes, and at SH tropics and subtropics, especially  
10 in the regions of subsidence. We find that lightning NO<sub>x</sub> emissions weaken both positive O<sub>3</sub>-CO  
11 correlations at mid- and high-latitudes and negative correlations in the tropics, and change weak  
12 positive correlations to negative in various areas. This result contrasts with that of previous studies.

13 This study demonstrates the utility of O<sub>3</sub>-CO correlations to constrain the sources of  
14 tropospheric O<sub>3</sub> in global 3-D models. Our model simulations driven by three input meteorological  
15 data sets show significantly different global and regional distributions of O<sub>3</sub> and CO concentrations  
16 during boreal summer. For instance, GMI/fvGCM simulations show higher O<sub>3</sub> concentrations in  
17 the NH and lower CO concentrations than other simulations. Despite such differences, all  
18 simulations show similar patterns of O<sub>3</sub>-CO correlations on a global scale. The regional features  
19 of the correlations, however, are often different due to the discrepancies in various meteorological  
20 processes (e.g., convection, STE, subsidence). In particular, GMI/MERRA simulates broader areas  
21 of strong negative O<sub>3</sub>-CO correlations at 618 hPa in the tropics than GMI/fvGCM and  
22 GMI/GEOS4 do due to stronger tropical convection in the LT/MT. In this sense, O<sub>3</sub>-CO  
23 correlations can be used to constrain better the sources of regional tropospheric O<sub>3</sub> in global models,

1 especially for convective regions than O<sub>3</sub> and CO observations individually. Future work, where  
2 additional meteorological archives (e.g., GFDL AM3, ECMWF ERA-Interim) may also be  
3 incorporated, should examine the driving factors for O<sub>3</sub>-CO correlations in other seasons.

Deleted: will

#### 4 5 **Data availability**

6 A description of the model output and observational data used in this paper can be found in Sect.  
7 2 and they are available upon request by contacting Hongyu Liu ([hongyu.liu-1@nasa.gov](mailto:hongyu.liu-1@nasa.gov)).

8  
9 **Acknowledgements.** This work was supported by the NASA Modeling, Analysis, and Prediction  
10 (MAP) program and NASA Atmospheric Composition Modeling and Analysis Program  
11 (ACMAP). NASA Center for Computational Sciences (NCCS) provided supercomputing  
12 resources. TES data products are distributed by NASA Langley Atmospheric Science Data Center.

#### 13 14 **References**

- 15  
16 Allen, D., Pickering, K., Duncan, B., and Damon, M.: Impact of lightning NO emissions on North  
17 American photochemistry as determined using the Global Modeling Initiative (GMI) model,  
18 *J. Geophys. Res.*, *115*, D22301, doi:10.1029/2010JD014062, 2010.
- 19 Anderson, B. E., Gregory, G. L., Barrick, J. D. W., Collins, J. E. Jr., Sachse, G. W., Bagwell, D.,  
20 Shipham, M. C., Bradshaw, J. D., and Sandholm, S. T.: The impact of U.S. continental  
21 outflow on ozone and aerosol distributions over the western Atlantic, *J. Geophys. Res.*,  
22 *98*(D12), 23,477–23,489, doi:10.1029/93JD01208, 1993.

1 Beer, R., Glavich, T. A., and Rider, D. M.: Tropospheric emission spectrometer for the Earth  
2 Observing System's Aura Satellite, *Appl. Optics*, *40*, 2356–2367, 2001.

3 Beer, R.: TES on the Aura mission: Scientific objectives, measurements, and analysis overview,  
4 *IEEE T. Geosci. Remote*, *44*, 1102–1105, doi:10.1109/tgrs.2005.863716, 2006.

5 Bowman, K. W., Steck, T., Worden, H. M., Worden, J., Clough, S., and Rodgers, C.: Capturing  
6 time and vertical variability of tropospheric ozone: A study using TES nadir retrievals, *J.*  
7 *Geophys. Res.*, *107*(D23), 4723, doi:10.1029/2002JD002150, 2002.

8 Bowman, K. W., et al.: Tropospheric emission spectrometer: Retrieval method and error analysis,  
9 *IEEE T. Geosci. Remote*, *44*, 1297–1307, doi:10.1109/tgrs.2006871234, 2006.

10 Benkovitz, C. M., Scholtz, M. T., Pacyna, J., Tarrasón, L., Dignon, J., Voldner, E. C., Spiro, P.  
11 A., Logan, J. A., and Graedel, T. E.: Global gridded inventories of anthropogenic emissions  
12 of sulfur and nitrogen, *J. Geophys. Res.*, *101*(D22), 29239–29253, doi:10.1029/96JD00126,  
13 1996.

14 Bey, I., Jacob, D.J., Yantosca, R.M., Logan, J.A., Field, B., Fiore, A.M., Li, Q., Liu, H., Mickley,  
15 L.J., and Schultz, M.: Global modeling of tropospheric chemistry with assimilated  
16 meteorology: Model description and evaluation, *J. Geophys. Res.*, *106*, 23,073–23,096, 2001.

17 Bloom, S., Silva, A. da, Dee, D., Bosilovich, M., Chern, J.-D., Pawson, S., Schubert, S.,  
18 Sienkiewicz, M., Stajner, I., Tan, W.-W., and Wu, M.-L.: Documentation and Validation of  
19 the Goddard Earth Observing System (GEOS) Data Assimilation System - Version 4.  
20 *Technical Report Series on Global Modeling and Data Assimilation* (Editor Max J. Suarez),  
21 NASA/TM-2005-104606, Vol. 26, NASA Goddard Space Flight Center, Greenbelt,  
22 Maryland, April 2005, 2005.

1 Chin, M., Jacob, D. J., Munger, J. W., Parrish, D. D., and Doddridge, B. G.: Relationship of ozone  
2 and carbon monoxide over North America, *J. Geophys. Res.*, *99*(D7), 14,565–14,573,  
3 doi:10.1029/94JD00907, 1994.

4 Chandra, S., Ziemke, J. R., Duncan, B. N., Diehl, T. L., Livesey, N. J., and Froidevaux, L.: Effects  
5 of the 2006 El Niño on tropospheric ozone and carbon monoxide: implications for dynamics  
6 and biomass burning, *Atmos. Chem. Phys.*, *9*, 4239-4249, doi:10.5194/acp-9-4239-2009,  
7 2009.

8 Collins Jr., J. E., Anderson, B. E., Sachse, G. W., J. Barrick, D. W., Wade, L. O., Burney, L. G.,  
9 and Hill, G. F.: Atmospheric fine structure during GTE TRACE A: Relationships among  
10 ozone, carbon monoxide, and water vapor, *J. Geophys. Res.*, *101*(D19), 24307–24316,  
11 doi:10.1029/96JD02180, 1996.

12 Considine, D. B., Bergmann, D. J., and Liu, H.: Sensitivity of Global Modeling Initiative  
13 chemistry and transport model simulations of radon-222 and lead-210 to input  
14 meteorological data, *Atmos. Chem. Phys.*, *5*, 3389-3406, doi:10.5194/acp-5-3389-2005,  
15 2005.

16 Considine, D. B., Logan, J. A., and Olsen, M. A.: Evaluation of near-tropopause ozone  
17 distributions in the Global Modeling Initiative combined stratosphere/troposphere model  
18 with ozonesonde data, *Atmos. Chem. Phys.*, *8*, 2365-2385, doi:10.5194/acp-8-2365-2008,  
19 2008.

20 Cooper, O. R., Moody, J. L., Parrish, D. D., Trainer, M., Holloway, J. S., Hübler, G., Fehsenfeld,  
21 F. C., and Stohl, A.: Trace gas composition of midlatitude cyclones over the western North  
22 Atlantic Ocean: A seasonal comparison of O<sub>3</sub> and CO, *J. Geophys. Res.*, *107*(D7),  
23 doi:10.1029/2001JD000902, 2002.

1 Dobb, J. E., Meeker, L. D., Finkel, R. C., Southon, J. R., Caffee, M. W., and Barrie, L. A.:  
2 Estimation of stratospheric input to the Arctic troposphere:  $^7\text{Be}$  and  $^{10}\text{Be}$  in aerosols at Alert,  
3 Canada, *J. Geophys. Res.*, *99*, 12,855-12,864, 1994.

4 Douglass, A.R., Prather, M.J., Hall, T.M., Strahan, S.E., Rasch, P.J., Sparling, L.C., Coy, L., and  
5 Rodriguez, J.M.: Choosing meteorological input for the global modeling initiative  
6 assessment of high-speed aircraft, *J. Geophys. Res.*, *104*(D22), 27,545-27,564, 1999.

7 Douglass, A. R., Stolarski, R. S., Strahan, S. E., and Connell, P. S.: Radicals and reservoirs in the  
8 GMI chemistry and transport model: Comparison to measurements, *J. Geophys. Res.*, *109*,  
9 D16302, doi:10.1029/2004JD004632, 2004.

10 Duncan, B. N., Martin, R., Staudt, A., Yevich, R., and Logan, J.: Interannual and Seasonal  
11 Variability of Biomass Burning Emissions Constrained by Satellite Observations, *J.*  
12 *Geophys. Res.*, *108*(D2), 4100, doi:10.1029/2002JD002378, 2003.

13 Duncan, B. N., Strahan, S. E., Yoshida, Y., Steenrod, S. D., and Livesey, N.: Model study of the  
14 cross-tropopause transport of biomass burning pollution, *Atmos. Chem. Phys.*, *7*, 3713-3736,  
15 doi:10.5194/acp-7-3713-2007, 2007a.

16 Duncan, B. N., Logan, J. A., Bey, I., Megretskaia, I. A., Yantosca, R. M., Novelli, P. C., Jones, N.  
17 B., and Rinsland, C. P.: Global budget of CO, 1988–1997: Source estimates and validation  
18 with a global model, *J. Geophys. Res.*, *112*, D22301, doi:10.1029/2007JD008459, 2007b.

19 Duncan, B. N., West, J. J., Yoshida, Y., Fiore, A. M., and Ziemke, J. R.: The influence of  
20 European pollution on ozone in the Near East and northern Africa, *Atmos. Chem. Phys.*, *8*,  
21 2267-2283, doi:10.5194/acp-8-2267-2008, 2008.

22 Fan, J. and Zhang, R.: Atmospheric oxidation mechanism of Isoprene, *Environ. Chem.*, *1*, 140-  
23 149, doi: 10.1071/EV04045, 2004.

1 Fehsenfeld, F. C., Daum, P., Leaitch, W. R., Trainer, M., Parrish, D. D., and Hübler, G.: Transport  
2 and processing of O<sub>3</sub> and O<sub>3</sub> precursors over the North Atlantic: An overview of the 1993  
3 North Atlantic Regional Experiment (NARE) summer intensive, *J. Geophys. Res.*, 101(D22),  
4 28,877–28,891, doi:10.1029/96JD01113, 1996.

5 Fishman, J., and Seiler, W.: Correlative nature of ozone and carbon monoxide in the troposphere:  
6 Implications for the tropospheric ozone budget, *J. Geophys. Res.*, 88, 3662–3670, 1983.

7 Fishman, J., Wozniak, A. E., and Creilson, J. K.: Global distribution of tropospheric ozone from  
8 satellite measurements using the empirically corrected tropospheric ozone residual  
9 technique: Identification of the regional aspects of air pollution, *Atmos. Chem. Phys.*, 3, 893-  
10 907, 2003.

11 Guenther, A., Karl, T., Harley, P., Wiedinmyer, C., Palmer, P.I., and Geron, C.: Estimates of global  
12 terrestrial isoprene emissions using MEGAN (Model of Emissions of Gases and Aerosols  
13 from Nature), *Atmos. Chem. Phys.*, 6, 3181-3210, 2006.

14 Hack, J. J.: Parameterization of moist convection in the National Center for Atmospheric Research  
15 Community Climate Model (CCM2), *J. Geophys. Res.*, 99, 5551–5568, 1994.

16 Honrath, R. E., Owen, R. C., Val Martín, M., Reid, J. S., Lapina, K., Fialho, P., Dziobak, M. P.,  
17 Kleissl, J., and Westphal, D. L.: Regional and hemispheric impacts of anthropogenic and  
18 biomass burning emissions on summertime CO and O<sub>3</sub> in the North Atlantic lower free  
19 troposphere, *J. Geophys. Res.*, 109, D24310, doi:10.1029/2004JD005147, 2004.

20 Hsu, J., Prather, M. J., Wild, O., Sundet, J. K., Isaksen, I. S. A., Browell, E. V., Avery, M. A., and  
21 Sachse, G. W.: Are the TRACE-P measurements representative of the western Pacific during  
22 March 2001?, *J. Geophys. Res.*, 109(D2), D02314, doi:10.1029/2003JD004002, 2004.

- 1 Jacob D. J., and Wofsy, S. C.: Budgets of Reactive Nitrogen, Hydrocarbons, and Ozone Over the  
2 Amazon Forest During the Wet Season, *J. Geophys. Res.*, *95*, 16,737-16,754, 1990.
- 3 Jacob, D. J., et al.: Evaluation and inter-comparison of global atmospheric transport models using  
4  $^{222}\text{Rn}$  and other short-lived tracers, *J. Geophys. Res.*, *102*, 5953-5970, 1997.
- 5 Jaffe, D. A., Honrath, R. E., Zhang, L., Akimoto, H., Shimizu, A., Mukai, H., Murano, K.,  
6 Hatakeyama, S., and Merrill, J.: Measurements of NO, NO<sub>y</sub>, CO and O<sub>3</sub> and estimation of  
7 the ozone production rate at Oki Island, Japan, during PEM-West, *J. Geophys. Res.*, *101*(D1),  
8 2037–2048, doi:10.1029/95JD01699, 1996.
- 9 Kim, P. S., Jacob, D. J., Liu, X., Warner, J. X., Yang, K., Chance, K., Thouret, V., and  
10 Nedelec, P.: Global ozone–CO correlations from OMI and AIRS: constraints on tropospheric  
11 ozone sources, *Atmos. Chem. Phys.*, *13*, 9321-9335, doi:10.5194/acp-13-9321-2013, 2013.
- 12 Kinnison, D. E., et al.: The Global Modeling Initiative assessment model: Application to high-  
13 speed civil transport perturbation, *J. Geophys. Res.*, *106*(D2), 1693–1711,  
14 doi:10.1029/2000JD900406, 2001.
- 15 Koch, D. M., and Mann, M. E.: Spatial and temporal variability of  $^{7}\text{Be}$  surface concentration,  
16 *Tellus, Ser. B*, *48*, 387-396, 1996.
- 17 Li, Q., Jacob, D. J., Bey, I., Palmer, P. I., Duncan, B. N., Field, B. D., Martin, R. V., Fiore, A.  
18 M., Yantosca, R. M., Parrish, D. D., Simmonds, P. G., and Oltmans, S. J.: Transatlantic  
19 transport of pollution and its effects on surface ozone in Europe and North America, *J.*  
20 *Geophys. Res.*, *107*(D13), doi:10.1029/2001JD001422, 2002.
- 21 Lin, S.-J., and Rood, R. B.: Multidimensional flux-form semi-Lagrangian transport schemes, *Mon.*  
22 *Weather Rev.*, *124*, 2046–2070, 1996.

- 1 Liu, H., Jacob, D. J., Bey, I., and Yantosca, R. M.: Constraints from  $^{210}\text{Pb}$  and  $^7\text{Be}$  on wet  
2 deposition and transport in a global three-dimensional chemical tracer model driven by  
3 assimilated meteorological fields, *J. Geophys. Res.*, *106*(D11), 12109–12128,  
4 doi:10.1029/2000JD900839, 2001.
- 5 Liu, H., Considine, D. B., Horowitz, L. W., Crawford, J. H., Rodriguez, J. M., Strahan, S. E.,  
6 Damon, M. R., Steenrod, S. D., Xu, X., Kouatchou, J., Carouge, C., and Yantosca, R. M.:  
7 Using beryllium-7 to assess cross-tropopause transport in global models, *Atmos. Chem.*  
8 *Phys.*, *16*, 4641-4659, doi:10.5194/acp-16-4641-2016, 2016.
- 9 Liu, J., Logan, J. A., Jones, D. B. A., Livesey, N. J., Megretskaja, I., Carouge, C., and Nedelec, P.:  
10 Analysis of CO in the tropical troposphere using Aura satellite data and the GEOS-Chem  
11 model: insights into transport characteristics of the GEOS meteorological products, *Atmos.*  
12 *Chem. Phys.*, *10*, 12207-12232, doi:10.5194/acp-10-12207-2010, 2010.
- 13 Logan, J. A. (1999), An analysis of ozonesonde data for the troposphere: Recommendations for  
14 testing 3-D models and development of a gridded climatology for tropospheric ozone, *J.*  
15 *Geophys. Res.*, *104*, 16 115–16 149.
- 16 Lopez, J. P., Luo, M., Christensen, L. E., Loewenstein, M., Jost, H., Webster, C. R., and Osterman,  
17 G.: TES carbon monoxide validation during two AVE campaigns using the Argus and  
18 ALIAS instruments on NASA's WB-57F, *J. Geophys. Res.*, *113*, D16S47,  
19 doi:10.1029/2007JD008811, 2008.
- 20 Luo, M., et al.: TES carbon monoxide validation with DACOM aircraft measurements during  
21 INTEX-B 2006, *J. Geophys. Res.*, *112*, D24S48, doi:10.1029/2007JD008803, 2007a,

Deleted: .

1 Luo, M., et al.: Comparison of carbon monoxide measurements by TES and MOPITT: Influence  
2 of a priori data and instrument characteristics on nadir atmospheric species retrievals, *J.*  
3 *Geophys. Res.*, 112, D09303, doi:10.1029/2006JD007663, 2007b.

Deleted: ,

4 Mao, H., and Talbot, R.: O<sub>3</sub> and CO in New England: Temporal variations and relationships, *J.*  
5 *Geophys. Res.*, 109, D21304, doi:10.1029/2004JD004913, 2004.

6 Mari, C., Jacob, D. J., and Bechtold, P.: Transport and scavenging of soluble gases in a deep  
7 convective cloud, *J. Geophys. Res.*, 105, 22,255-22,267, 2000.

8 Mauzerall, D. L., Narita, D., Akimoto, H., Horowitz, L., Walters, S., Hauglustaine, D. A., and  
9 Brasseur, G.: Seasonal characteristics of tropospheric ozone production and mixing ratios  
10 over East Asia: A global three-dimensional chemical transport model analysis, *J. Geophys.*  
11 *Res.*, 105(D14), 17,895–17,910, doi:10.1029/2000JD900087, 2000.

12 Moorthi S. and Suarez, M. J.: Relaxed Arakawa-Shubert. A Parameterization of moist convection  
13 for general circulation models, *Mon. Weather Rev.*, 120, 978-1002, 1992.

14 Naja, M., Lal, S., and Chand, D.: Diurnal and seasonal variabilities in surface ozone at a high  
15 altitude site Mt Abu (24.6 degrees N, 72.7 degrees E, 1680 m asl) in India, *Atmos. Environ.*,  
16 37, 4205–4215, doi:10.1016/S1352-2310(03)00565-X, 2003.

17 Nassar, R., et al.: Validation of Tropospheric Emission Spectrometer (TES) nadir ozone profiles  
18 using ozonesonde measurements, *J. Geophys. Res.*, 113, D15S17,  
19 doi:10.1029/2007JD008819, 2008.

20 Osterman, G. B., Kulawik, S. S., Worden, H., Richards, N. A., Fisher, B. M., Eldering, A.,  
21 Shephard, M. W., Froidevaux, L., Labow, G., Luo, M., Herman, R. L., Bowman, K. W., and  
22 Thompson, A. M.: Validation of Tropospheric Emission Spectrometer (TES) measurements

Deleted: Mao, H., and Talbot, R.: O<sub>3</sub> and CO in New England:  
Temporal variations and relationships, *J. Geophys. Res.*, 109,  
D21304, doi:10.1029/2004JD004913, 2004.¶

1 of the total, stratospheric, and tropospheric column abundance of ozone, *J. Geophys. Res.*,  
2 113, D15S16, doi:10.1029/2007JD008801, 2008.

3 Parrington, M., Jones, D. B. A., Bowman, K. W., Horowitz, L. W., Thompson, A. M., Tarasick,  
4 D. W., and Witte, J. C.: Estimating the summertime tropospheric ozone distribution over  
5 North America through assimilation of observations from the Tropospheric Emission  
6 Spectrometer, *J. Geophys. Res.*, 113, D18307, doi:10.1029/2007JD009341, 2008.

7 Parrish, D. D., Holloway, J. S., Trainer, M., Murphy, P. C., Forbes, G. L., and Fehsenfeld, F. C.:  
8 Export of North American Ozone Pollution to the North Atlantic Ocean, *Science*, 259, 1436–  
9 1439, 1993.

10 Parrish, D. D., Trainer, M., Holloway, J. S., Yee, J. E., Warshawasky, M. S., and Fehsenfeld, F.  
11 C.: Relationships between ozone and carbon monoxide at surface sites in the North Atlantic  
12 region, *J. Geophys. Res.*, 103(D11), 13357–13376, 1998.

13 Real, E., Law, K. S., Schlager, H., Roiger, A., Huntrieser, H., Methven, J., Cain, M., Holloway, J.,  
14 Neuman, J. A., Ryerson, T., Flocke, F., Gouw, J. de, Atlas, E., Donnelly, S., and Parrish, D.:  
15 Lagrangian analysis of low altitude anthropogenic plume processing across the North  
16 Atlantic, *Atmos. Chem. Phys.*, 8, 7737–7754, doi:10.5194/acp-8-7737-2008, 2008.

17 Rotman, D. A., et al.: Global Modeling Initiative assessment model: Model description, integration,  
18 and testing of the transport shell, *J. Geophys. Res.*, 106, 1669–1691, 2001.

19 Schoeberl, M. R., Duncan, B. N., Douglass, A. R., Waters, J., Livesey, N., Read, W., and Filipiak,  
20 M.: The carbon monoxide tape recorder, *Geophys. Res. Lett.*, 33, L12811,  
21 doi:10.1029/2006GL026178, 2006.

22 Seinfeld, J. H., and Pandis, S. N.: Atmospheric Chemistry and Physics, *Wiley*, New York, 1998.

1 Shim, C., Li, Q., Luo, M., Kulawik, S., Worden, H., Worden, J., Eldering, A., Diskin, G., Sachse,  
2 G., Weinheimer, A., Knapp, D., Montzca, D., and Campos, T.: Satellite observations of  
3 Mexico City pollution outflow from the Tropospheric Emissions Spectrometer (TES),  
4 *Atmos. Environ.*, *43*, 1540–1547, doi:10.1016/j.atmosenv.2008.11.026, 2009.

5 Shindell, D. T., et al.: Multimodel simulations of carbon monoxide: Comparison with observations  
6 and projected near-future changes, *J. Geophys. Res.*, *111*, D19306,  
7 doi:10.1029/2006JD007100, 2006.

8 Strahan, S. E., Duncan, B. N., and Hoor, P.: Observationally derived transport diagnostics for the  
9 lowermost stratosphere and their application to the GMI chemistry and transport model,  
10 *Atmos. Chem. Phys.*, *7*, 2435–2445, doi:10.5194/acp-7-2435-2007, 2007.

11 Thompson, A. M., Pickering, K. E., McNamara, D. P., Schoeberl, M. R., Hudson, R. D., Kim, J.  
12 H., Browell, E. V., Kirchhoff, V. W. J. H., and Nganga, D.: Where did tropospheric ozone  
13 over southern Africa and the tropical Atlantic come from in October 1992? Insights from  
14 TOMS, GTE TRACE A, and SAFARI 1992, *J. Geophys. Res.*, *101*(D19), 24,251–24,278,  
15 doi:10.1029/96JD01463, 1996.

16 Thompson, A. M., Witte, J. C., McPeters, R. D., et al.: Southern Hemisphere Additional  
17 Ozonesondes (SHADOZ) 1998–2000 tropical ozone climatology – 1. Comparison with  
18 Total Ozone Mapping Spectrometer (TOMS) and ground-based measurements, *J. Geophys.*  
19 *Res.*, *108*(D2), 8238, doi:10.1029/2001JD000967, 2003.

20 Tsutsumi, Y., and Matsueda, H.: Relationship of ozone and CO at the summit of Mt. Fuji (35.35  
21 degrees N, 138.73 degrees E, 3776 m above sea level) in summer 1997, *Atmos. Environ.*, *34*,  
22 553– 561, 2000.

1 Voulgarakis, A., Telford, P. J., Aghedo, A. M., Braesicke, P., Faluvegi, G., Abraham, N. L.,  
2 Bowman, K. W., Pyle, J. A., and Shindell, D. T.: Global multi-year O<sub>3</sub>-CO correlation  
3 patterns from models and TES satellite observations, *Atmos. Chem. Phys.*, *11*, 5819-5838,  
4 doi:10.5194/acp-11-5819-2011, 2011.

5 Wang, T., Wong, H. L. A., Tang, J., Ding, A., Wu, W. S., and Zhang, X. C.: On the origin of  
6 surface ozone and reactive nitrogen observed at a remote mountain site in the northeastern  
7 Qinghai-Tibetan Plateau, western China, *J. Geophys. Res.*, *111*, D08303,  
8 doi:10.1029/2005JD006527, 2006.

9 Worden, J., Kulawik, S. S., Shephard, M. W., Clough, S. A., Worden, H., Bowman, K., and  
10 Goldman, A.: Predicted errors of tropospheric emission spectrometer nadir retrievals from  
11 spectral window selection, *J. Geophys. Res.*, *109*, D09308, doi:10.1029/2004JD004522,  
12 2004.

13 Worden, H. M., et al.: Comparisons of Tropospheric Emission Spectrometer (TES) ozone profiles  
14 to ozonesondes: Methods and initial results, *J. Geophys. Res.*, *112*, D03309,  
15 doi:10.1029/2006JD007258, 2007.

16 Yevich, R., and Logan, J. A.: An assesment of biofuel use and burning of agricultural waste in the  
17 developing world, *Global Biogeochem. Cycles*, *17*, (4), 1095, doi:10.1029/2002GB001952,  
18 2003.

19 Zhang, G. J., and McFarlane, N. A.: Sensitivity of climate simulations to the parameterization of  
20 cumulus convection in the Canadian Climate Centre general circulation model, *Atmos.*  
21 *Ocean.*, *33*, 407–446, 1995.

22 Zhang, L., Jacob, D. J., Bowman, K. W., Logan, J. A., Turquety, S., Hudman, R. C., Li, Q., Beer,  
23 R., Worden, H. M., Rinsland, C. P., Kulawik, S. S., Lampel, M. C., Shephard, M. W., Fisher,

1 B. M., Eldering, A., and Avery, M. A.: Ozone-CO correlations determined by the TES  
2 satellite instrument in continental outflow regions, *Geophys. Res. Lett.*, *33*, L18804,  
3 doi:10.1029/2006GL026399, 2006.

4 Zhang, L., Li, Q. B., Jin, J., Liu, H., Livesey, N., Jiang, J. H., Mao, Y., Chen, D., Luo, M. , and  
5 Chen, Y.: Impacts of 2006 Indonesian fires and dynamics on tropical upper tropospheric  
6 carbon monoxide and ozone, *Atmos. Chem. Phys.*, *11*, 10929-10946, doi:10.5194/acp-11-  
7 10929-2011, 2011 .

8 Zhang, L., Li, Q. B., Murray, L. T., Luo, M., Liu, H., Jiang, J. H., Mao, Y., Chen, D., Gao, M., and  
9 Livesey, N.: A tropospheric ozone maximum over the equatorial Southern Indian Ocean,  
10 *Atmos. Chem. Phys.*, *12*, 4279-4296, doi:10.5194/acp-12-4279-2012, 2012.

11 Ziemke, J.R., Chandra, S., Duncan, B. N., Froidevaux, L., Bhartia, P. K., Levelt, P. F., and Waters,  
12 J. W.: Tropospheric ozone determined from Aura OMI and MLS: Evaluation of  
13 measurements and comparison with the Global Modeling Initiative's Chemical Transport  
14 Model, *J. Geophys. Res.*, *111*, D19303, doi:10.1029/2006JD007089, 2006.

15  
16  
17  
18  
19  
20  
21  
22  
23  
24  
25

1  
2  
3  
4  
5  
6  
7  
8  
9  
10  
11  
12  
13  
14  
15  
16  
17  
18  
19  
20  
21  
22  
23  
24  
25  
26

**Table 1.** Global lightning NO<sub>x</sub> emissions (Tg N/mon) during May – August in GMI CTM driven by three meteorological data sets (fvGCM, GEOS4, and MERRA)

	May	June	July	August
fvGCM	0.57 (0.03 <sup>a</sup> )	0.65 (0.02)	0.80 (0.03)	0.78 (0.05)
GEOS4	0.64 (0.05)	0.73 (0.07)	0.82 (0.03)	0.72 (0.05)
MERRA	0.49 (0.07)	0.69 (0.07)	0.81 (0.03)	0.78(0.04)

Formatted Table

<sup>a</sup> Values in parenthesis denote lightning NO<sub>x</sub> emissions between 10°S and 70°S.

1  
2  
3  
4  
5  
6  
7  
8  
9

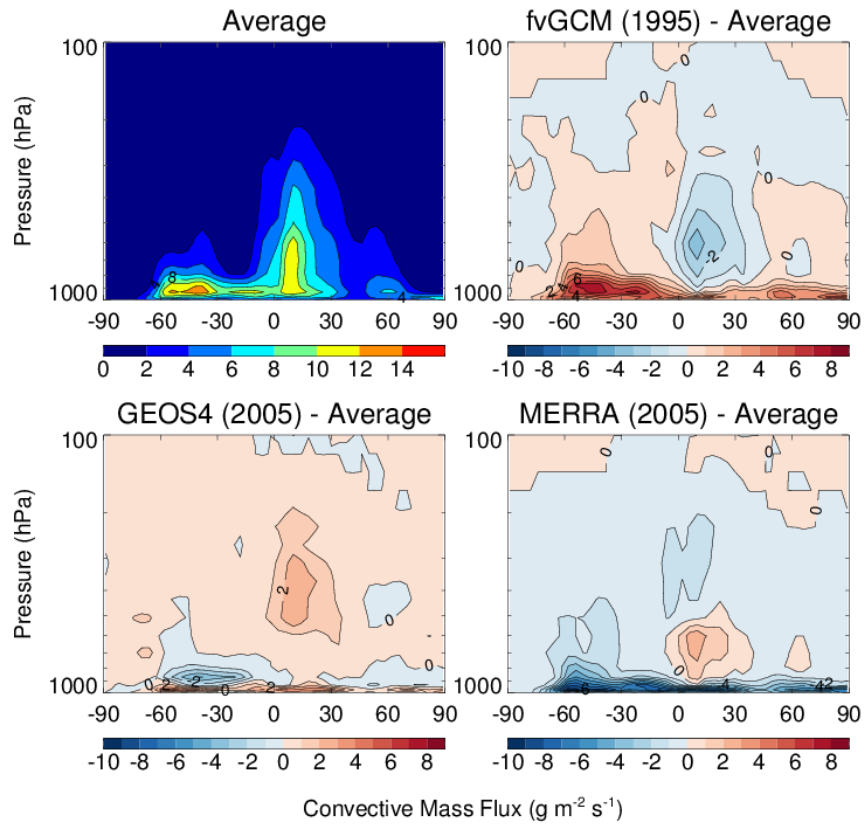
**Table 2.** Mean differences (ppbv) between GMI-simulated O<sub>3</sub> and ozonesonde observations at 500 hPa and 200 hPa, respectively.

Ozonesonde Station	GMI/fvGCM - sonde		GMI/GEOS4 - sonde		GMI/MERRA - sonde	
	500 hPa	200 hPa	500 hPa	200 hPa	500 hPa	200 hPa
Resolute (75°N, 95°W)	8.53	48.37	1.72	-65.79	-7.33	-85.56
Churchill (59°N, 147°W)	10.52	129.41	-0.30	-8.82	-8.98	-38.87
Hohenpeissenberg (48°N, 11°E)	9.53	43.85	4.81	33.60	-3.15	2.20
Sapporo (43°N, 141°E)	14.07	41.76	5.58	39.03	-2.95	34.90
Wallops Island (38°N, 76°W)	9.21	-11.07	13.14	-14.83	6.41	-6.91
Paramaribo (6°N, 55°W)	-9.46	-8.11	-10.74	-19.83	-12.84	7.38
Nairobi (1°S, 37°E)	-10.94	-15.53	-4.35	-15.91	-1.62	-8.20
Samoa (14°S, 170°W)	-5.33	-7.27	-2.45	-4.01	17.22	27.85
Reunion Island (21°S, 55°E)	-11.49	-17.30	0.51	-2.50	8.38	16.91

- Formatted: Font: Bold
- Deleted: The m
- Deleted: in
- Formatted: Subscript
- Deleted: ozonesonde
- Deleted: representing MT and UT,
- Formatted Table
- Deleted: -
- Formatted: Centered
- Deleted: ¶

1  
2

Deleted: ¶



3

4

5

**Fig. 1.** Latitude-height cross sections of zonal mean convective mass fluxes during July-August. The plot shows the values averaged over the fvGCM (1995), GEOS4 (2005), and MERRA (2005) meteorological data sets, as well as differences from the average.

Deleted: ure

8

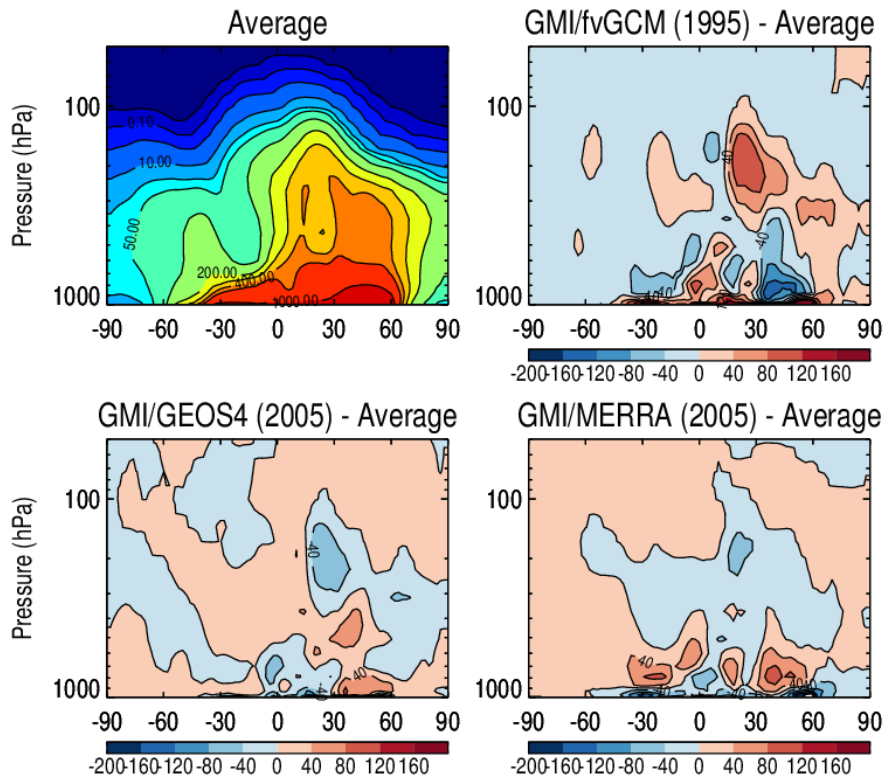
9

10

11

12

1



2

3

4

**Fig. 2.** Latitude-height cross sections of zonal mean  $^{222}\text{Rn}$  concentrations ( $\text{mBq SCM}^{-1}$ ) as simulated by GMI for July-August. The plot shows the values averaged over three simulations driven by the fvGCM (1995), GEOS4 (2005), and MERRA (2005) meteorological data sets, as well as differences of each simulation from the average.

8

9

10

11

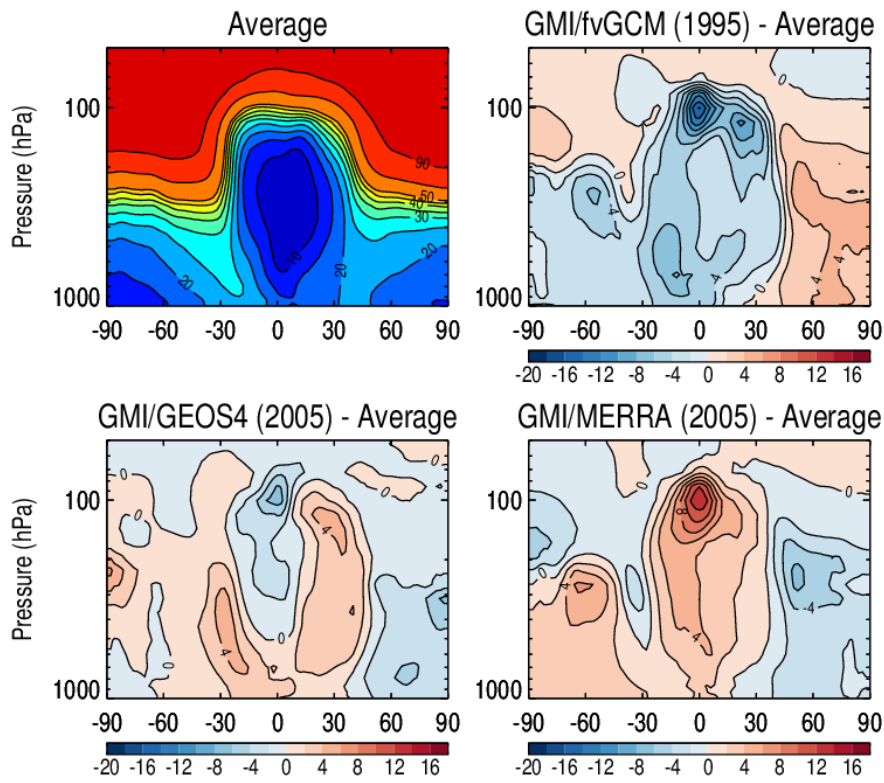
12

13

14

Deleted: ure

1  
2



3  
4

5 **Fig. 3.** Same as Fig. 2, but for stratospheric fraction (%) of zonal mean tropospheric <sup>7</sup>Be  
6 concentrations.

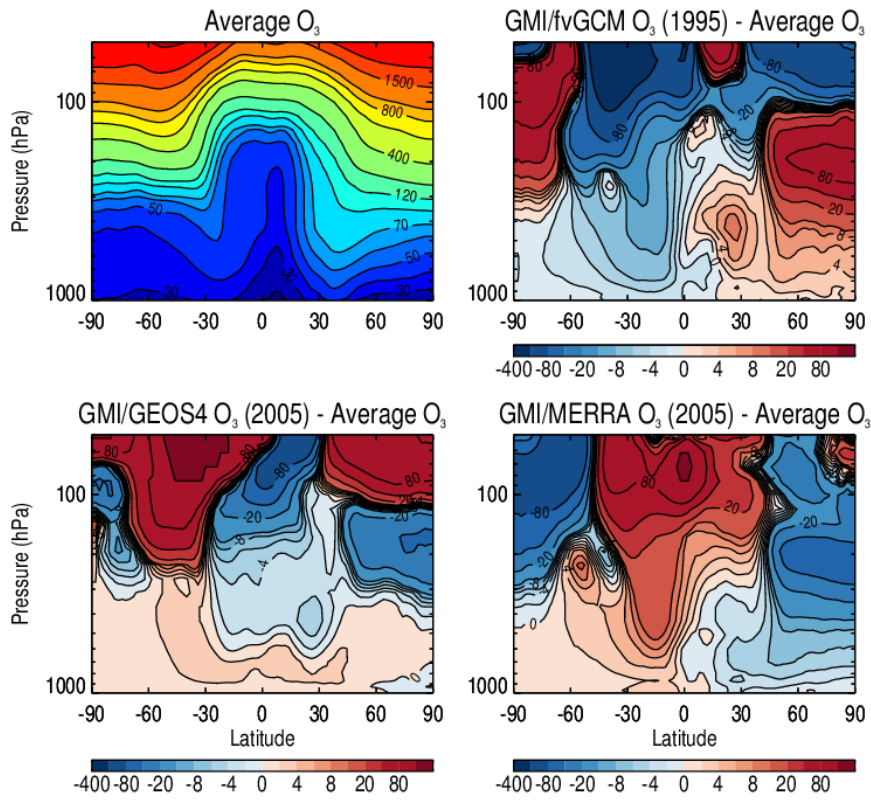
Deleted: ure

Formatted: Font: Not Bold

Deleted: ure

7  
8  
9  
10  
11  
12  
13

1  
2



3  
4  
5  
6  
7  
8  
9  
10  
11

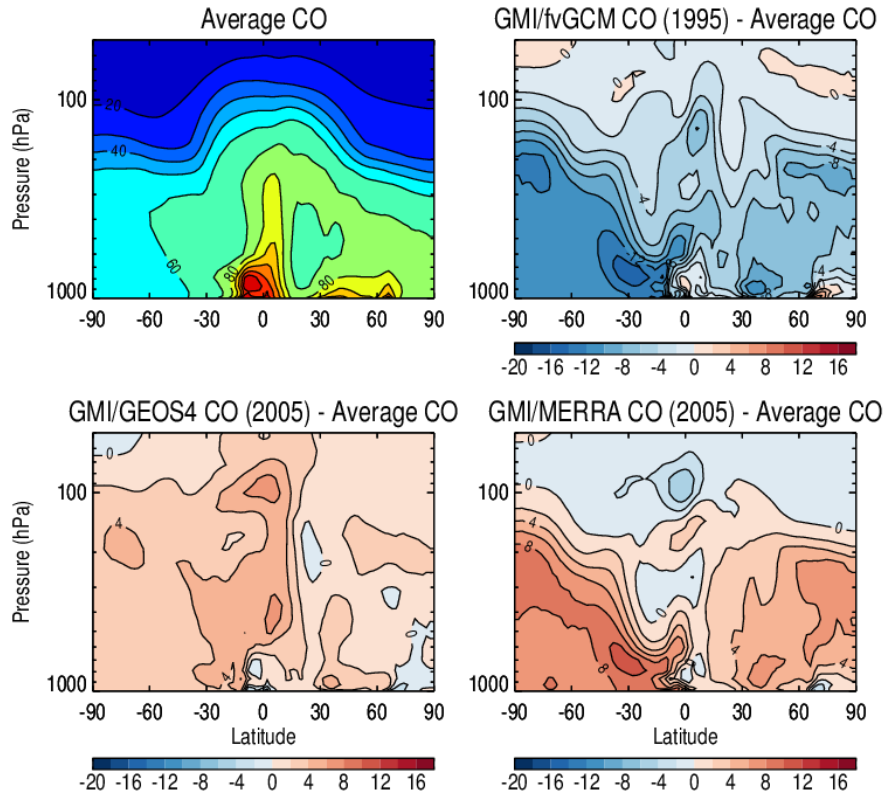
**Fig. 4.** Same as Fig. 2, but for zonal mean ozone mixing ratios (ppbv).

**Deleted:** ure

**Formatted:** Font: Not Bold

**Deleted:** ure

1



2

3

4

5

6

7

8

9

10

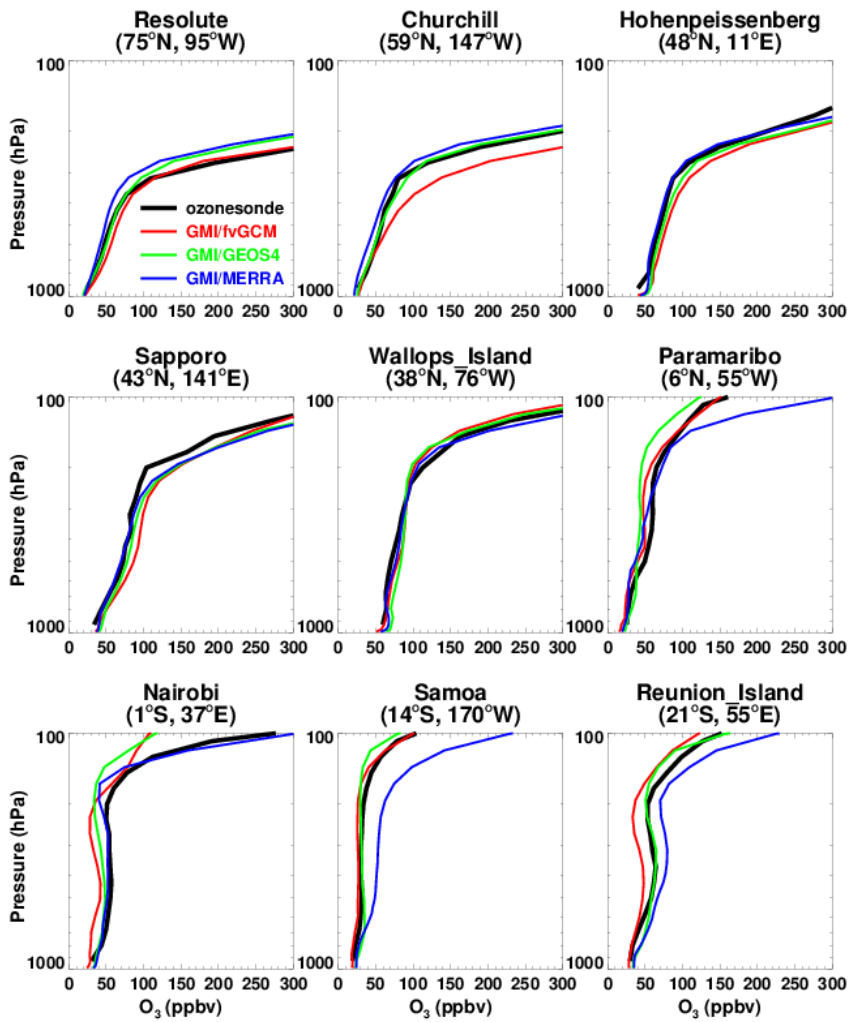
11

**Fig. 5.** Same as Fig. 2, but for zonal mean CO mixing ratios (ppbv).

Deleted: ure

Deleted: Figure

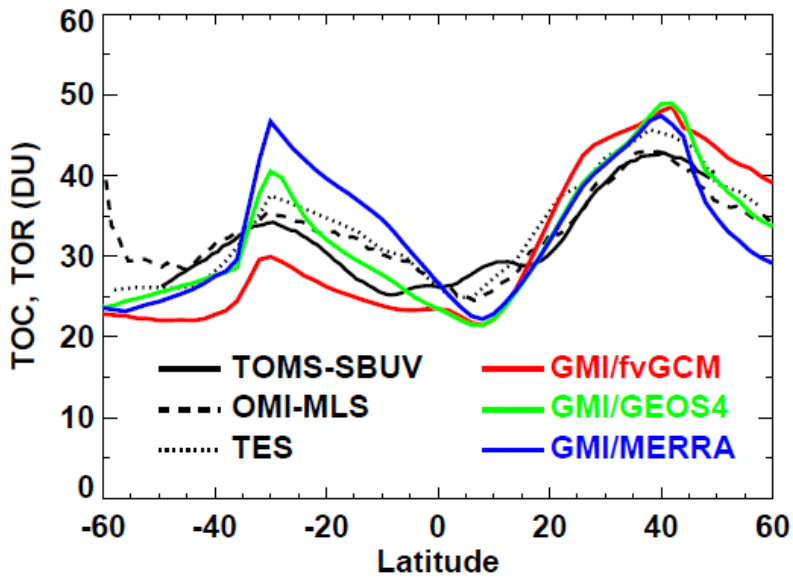
Formatted: Font: Not Bold



1  
2  
3  
4  
5  
6  
7

**Fig. 6.** Comparisons of GMI simulated tropospheric ozone profiles (color lines) with ozonesonde observations (black line) for a range of latitudes. The model is driven by the fvGCM, GEOS4, and MERRA meteorological fields. Values are July–August average.

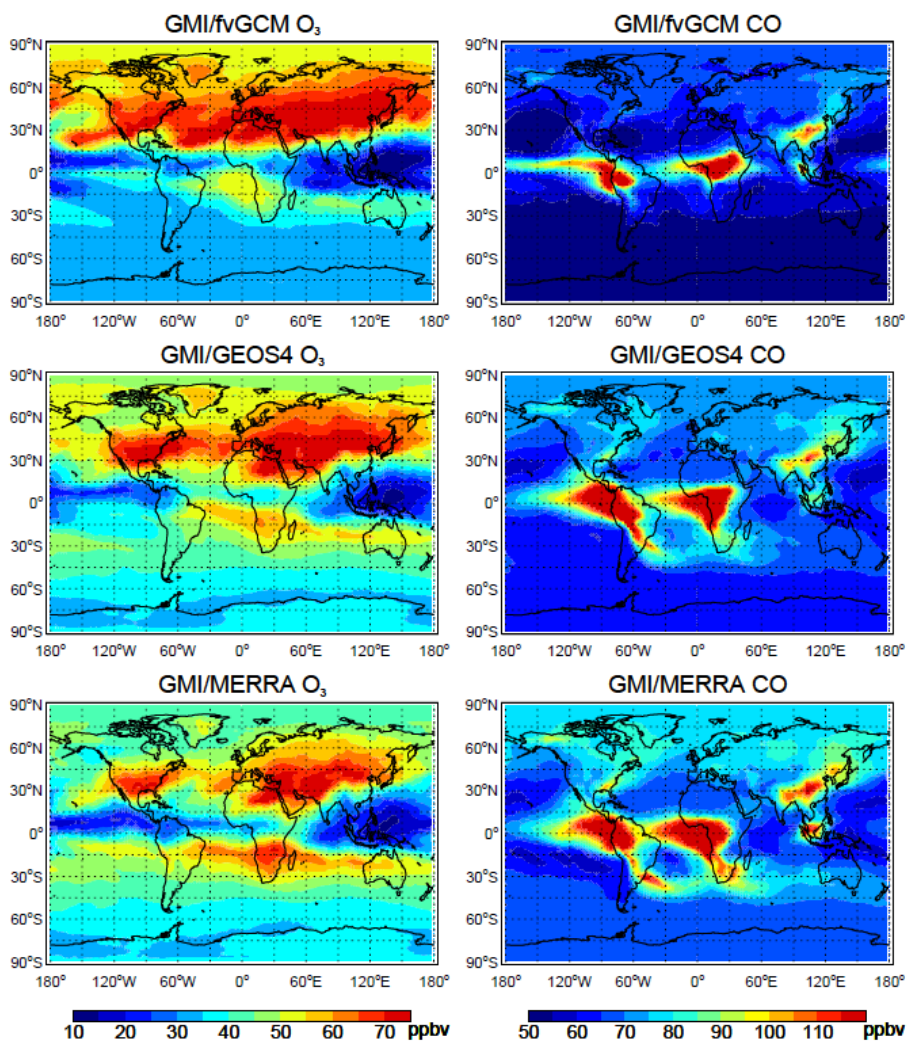
Deleted: ure



1  
2  
3  
4  
5  
6  
7

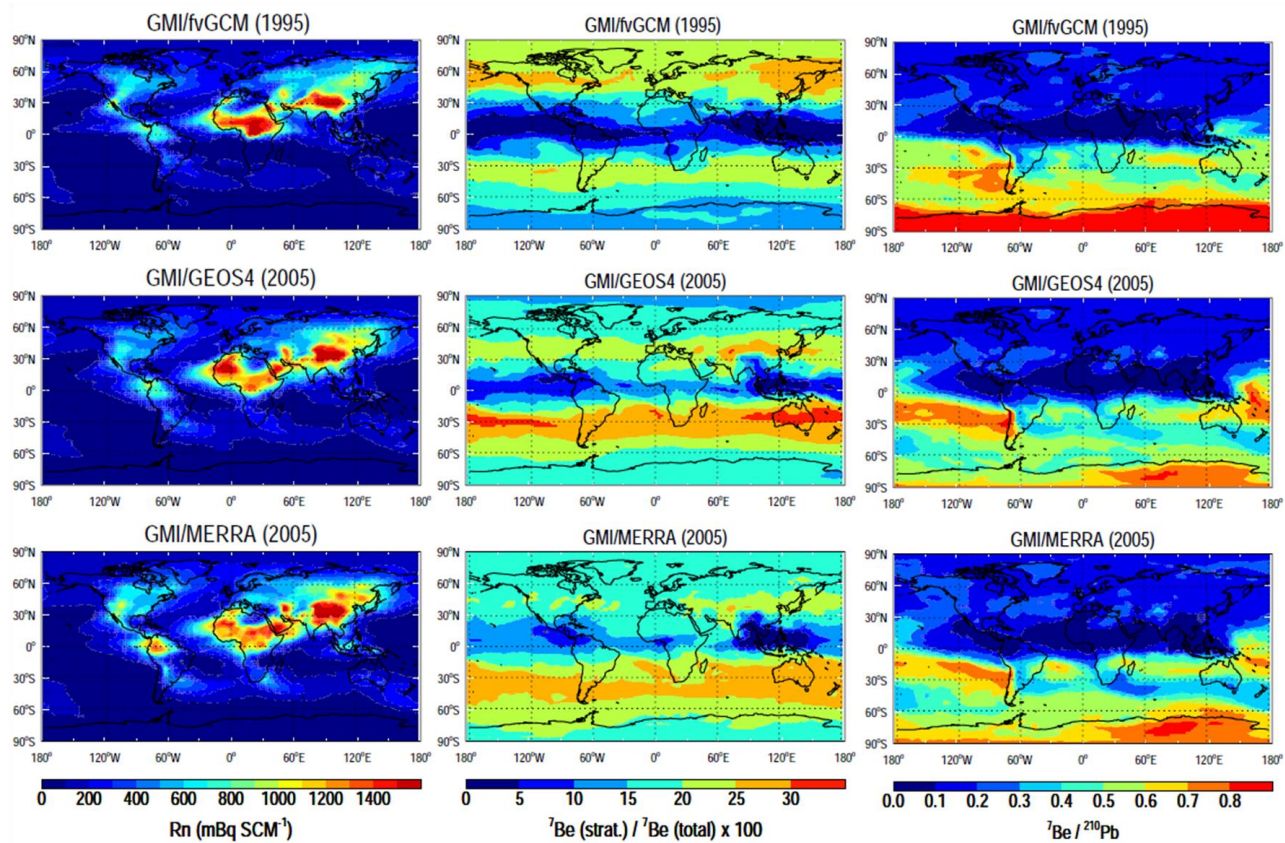
**Fig. 7.** GMI simulated zonal mean tropospheric ozone columns (TOCs) compared with tropospheric ozone residuals (TORs) determined from TOMS/SBUV (July–August 1979–2005 multi-year average) (Fishman et al., 2003), OMI/MLS (July–August 2005 average) (Ziemke et al., 2006), and TOCs determined from TES retrievals (July–August 2005 average).

Deleted: ure



4 **Fig. 8.** July-August mean mixing ratios of O<sub>3</sub> and CO (ppbv) at 618 hPa as simulated by GMI  
 5 CTM driven by three meteorological datasets (1995 for fvGCM, 2005 for GEOS4 and MERRA).

Deleted: ure

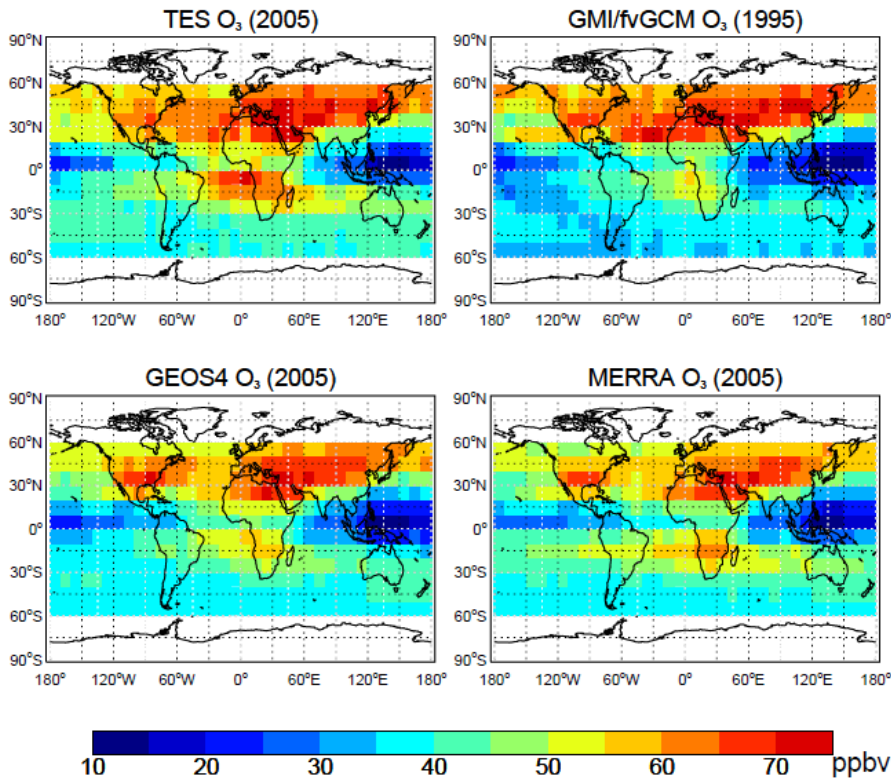


1  
2  
3  
4  
5

**Fig. 9.** Mean  $^{222}\text{Rn}$  concentrations ( $\text{mBq SCM}^{-1}$ ) (left column), stratospheric fraction (%) of tropospheric  $^7\text{Be}$  concentrations (middle column), and ratios of  $^7\text{Be}$  to  $^{210}\text{Pb}$  volume mixing ratios (right column) at 618 hPa in the GMI model driven by the fvGCM (1995), GEOS4 (2005), and MERRA (2005) meteorological data sets for the period of July - August.

Deleted: ure

1  
2



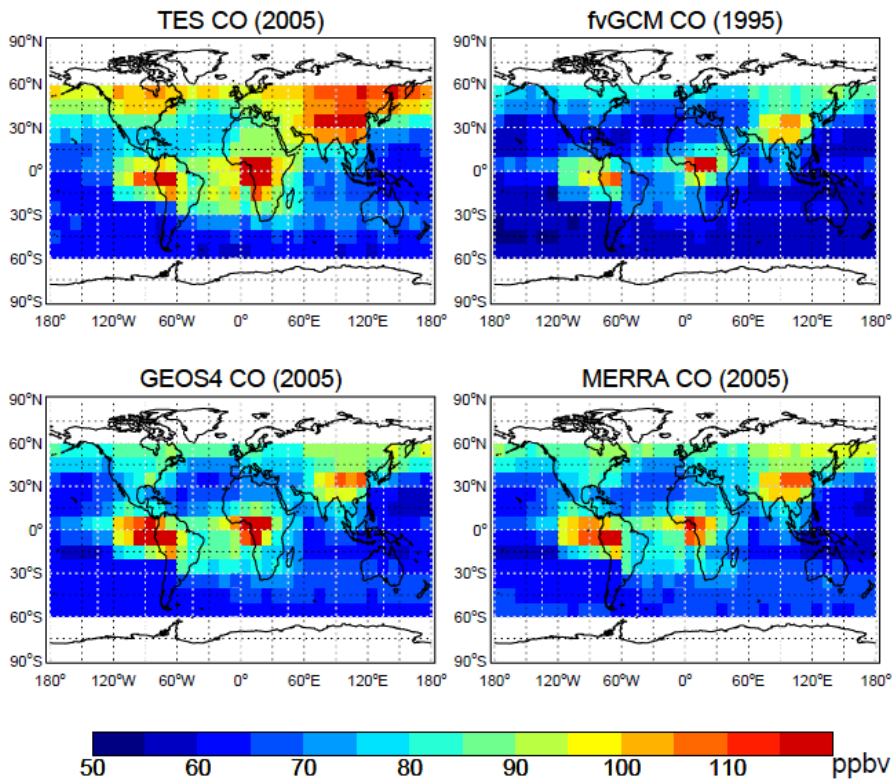
3  
4  
5

6 **Fig. 10.** Mean mixing ratios of O<sub>3</sub> at 618 hPa observed by TES during July- August 2005 and  
7 corresponding GMI CTM results with 3-hourly output sampled along the TES orbit tracks. TES  
8 averaging kernels and *a priori* were applied to the model output. Results are averaged into 10°×10°  
9 grid cells.

Deleted: ure

10  
11  
12  
13

1  
2  
3



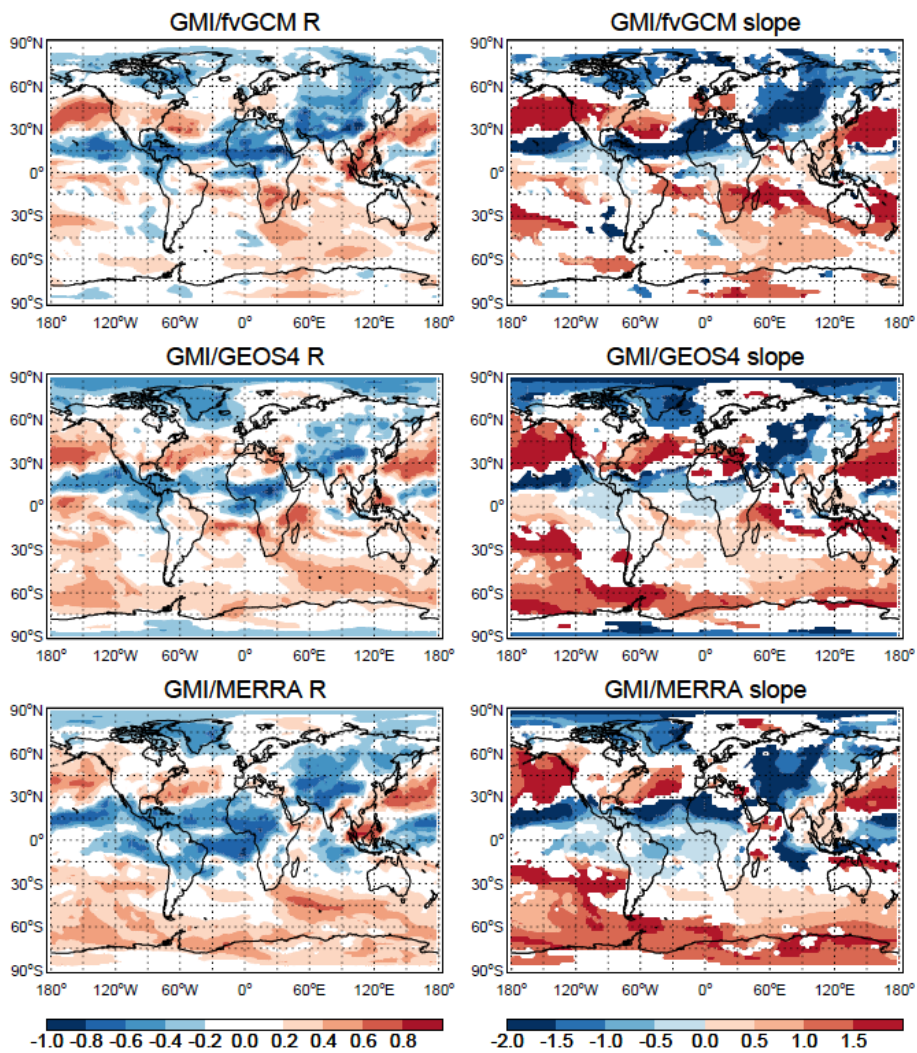
4  
5  
6  
7  
8

Fig. 11. Same as Fig. 10, but for CO.

Deleted: ure

Formatted: Font: Not Bold

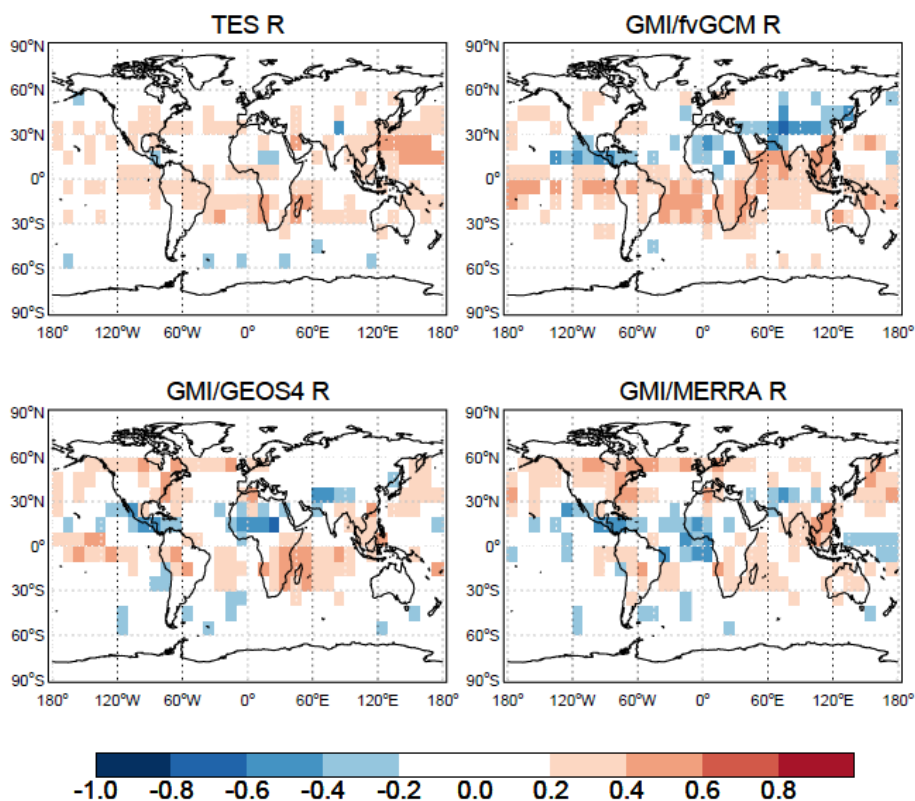
Deleted: ure



1  
2  
3  
4  
5  
6  
7

**Fig. 12.**  $O_3$ -CO correlation coefficients (R) and linear regression slopes ( $dO_3/dCO$ ) at 618 hPa in the GMI model driven by the fvGCM (1995), GEOS4 (2005), and MERRA (2005) meteorological fields. Results are calculated in  $2^\circ \times 2.5^\circ$  grid cells using 3-hourly model output and the reduced major axis method. White areas denote absolute values of  $O_3$ -CO correlation coefficients less than 0.2.

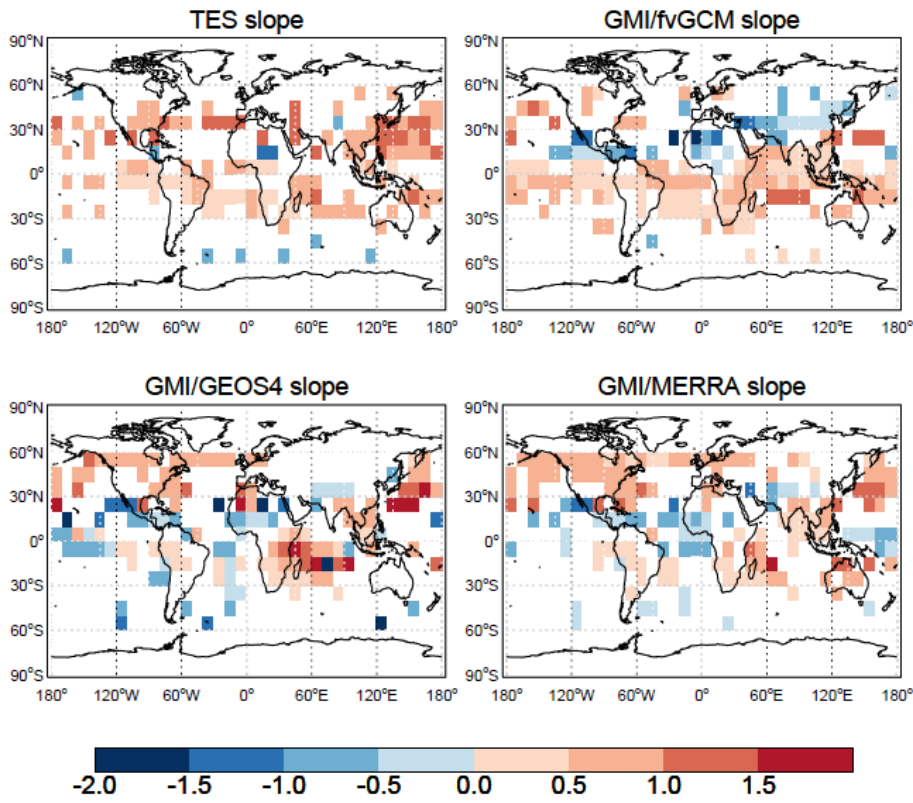
Deleted: ure



1  
2  
3

4 **Fig. 13.** O<sub>3</sub>-CO correlation coefficients (R) at 618 hPa as determined by O<sub>3</sub> and CO observations  
 5 from TES during July – August 2005, and corresponding GMI CTM results with 3-hourly output  
 6 sampled along the TES orbit tracks. TES averaging kernels, spectral errors, and a priori are applied.  
 7 Results are calculated in 10°×10° grid cells. White areas denote absolute values of O<sub>3</sub>-CO  
 8 correlation coefficients less than 0.2.

Deleted: ure



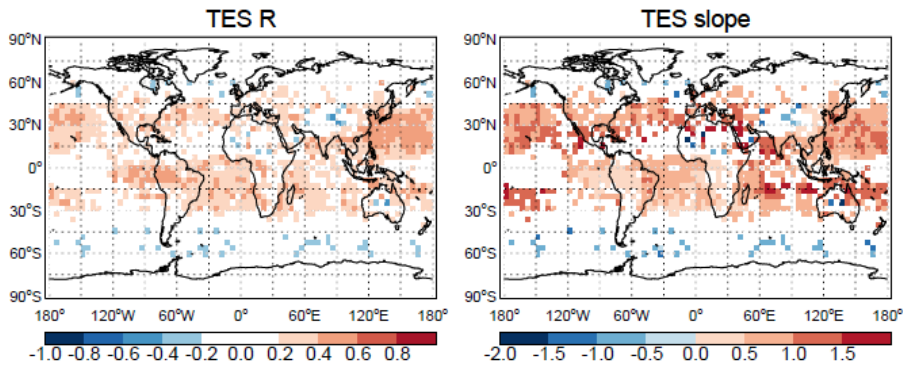
1  
2  
3  
4  
5  
6

Fig. 14. Same as Fig. 13, but for linear regression slopes  $dO_3/dCO$ .

Deleted: ure

Formatted: Font: Not Bold

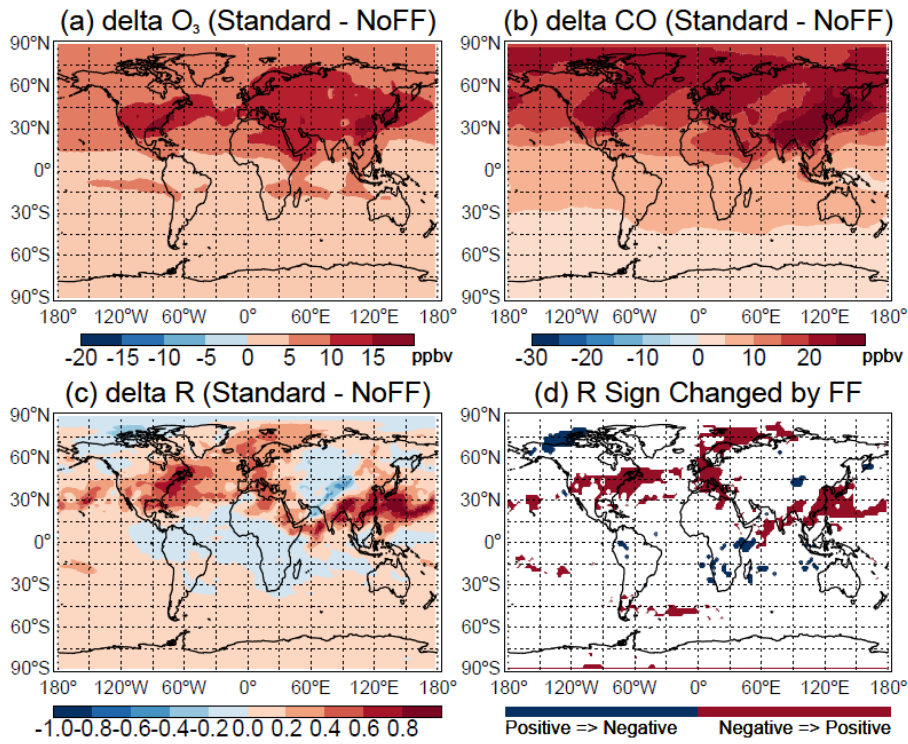
Deleted: ure



1  
2  
3  
4  
5  
6  
7  
8

**Fig. 15.** O<sub>3</sub>-CO correlation coefficients (R) and linear regression slopes (dO<sub>3</sub>/dCO) at 618 hPa as determined by O<sub>3</sub> and CO observations from TES during July–August, 2005 – 2009. Results are calculated in 4°×5° grid cells. White areas denote absolute values of O<sub>3</sub>-CO correlation coefficients less than 0.2.

Deleted: ure



1  
2  
3  
4  
5  
6  
7  
8  
9

**Fig. 16.** Sensitivity of O<sub>3</sub>, CO, and their correlations to fossil fuel (FF) emissions during July – August 2005. The plots show the mean differences in (a) O<sub>3</sub>, (b) CO mixing ratios (ppbv), and (c) O<sub>3</sub>-CO correlation coefficients (R) at 618 hPa between the standard GMI/MERRA simulation and a simulation where fossil fuel emissions are suppressed (NoFF) in the model. Also shown in (d) are the areas with changed correlation signs. Results are calculated using 3-hourly model output.

Deleted: ure

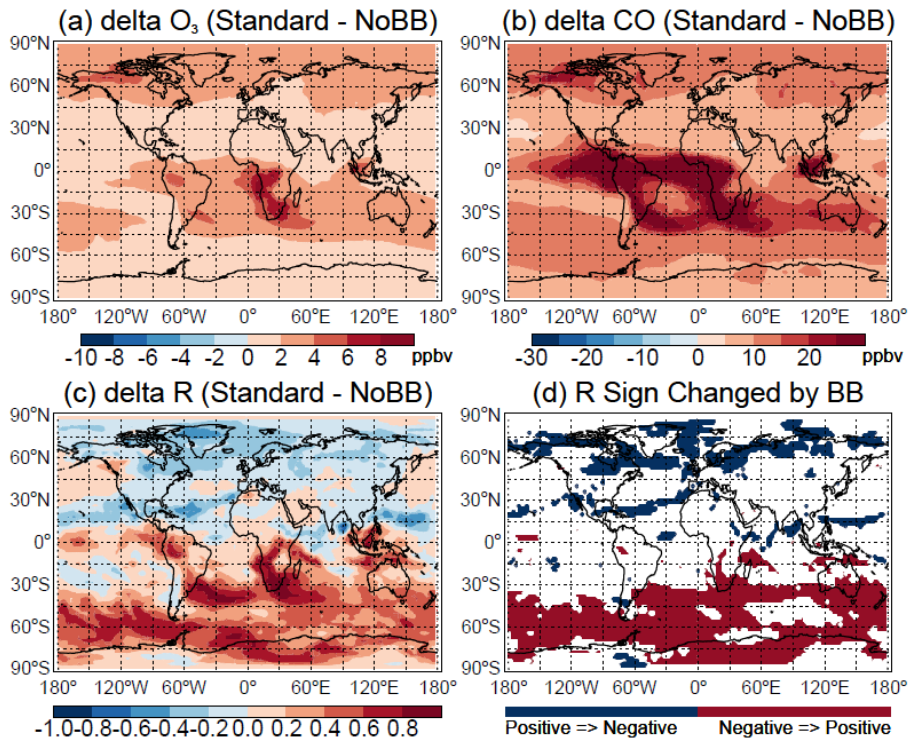
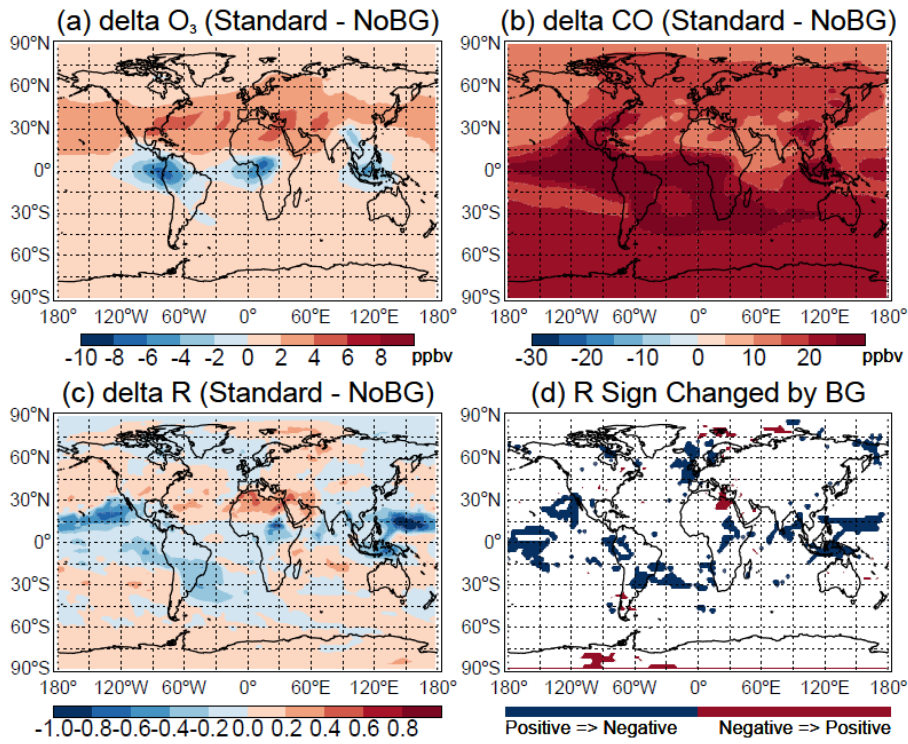


Fig. 17. Same as Fig. 16, but for the sensitivity of O<sub>3</sub>, CO, and their correlations at 618 hPa to biomass burning (BB) emissions.

Deleted: ure

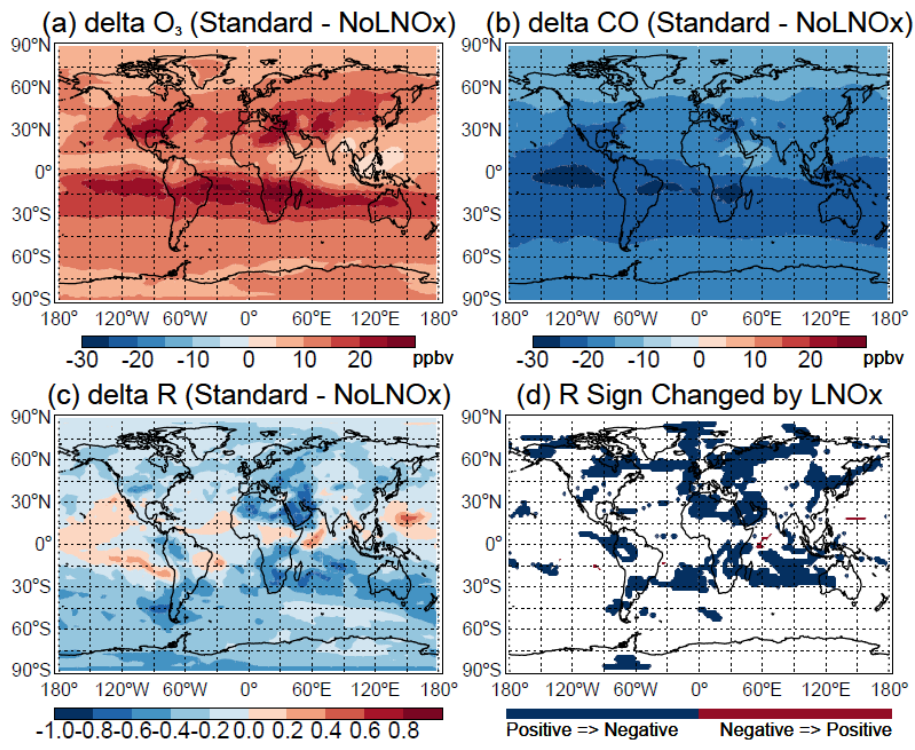
Deleted: ure



**Fig. 18.** Same as Fig. 16, but for the sensitivity of O<sub>3</sub>, CO, and their correlations at 618 hPa to biogenic (BG) emissions.

Deleted: ure

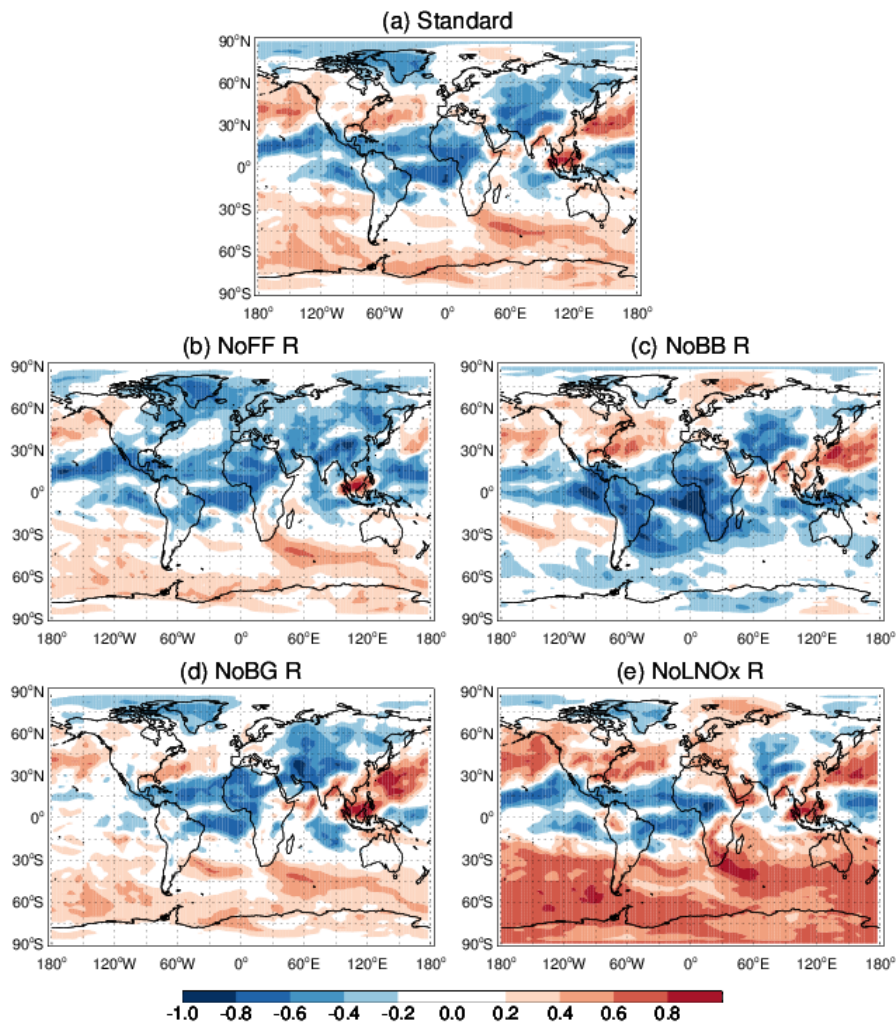
Deleted: ure



1  
2  
3  
4  
5  
6

**Fig. 19.** Same as Fig. 16, but for the sensitivity of O<sub>3</sub>, CO, and their correlations at 618 hPa to lightning NO<sub>x</sub> (LNO<sub>x</sub>) emissions.

Deleted: ure  
Deleted: ure



1

2

3 **Fig. 20.** GMI/MERRA-simulated  $O_3$ -CO correlations (R) at 618 hPa (a) in the standard simulation  
 4 and (b) - (e) when fossil fuel (FF), biomass burning (BB), biogenic (BG), and lightning NO<sub>x</sub>  
 5 (LNO<sub>x</sub>) emissions are individually suppressed (NoFF, NoBB, NoBG, and NoLNO<sub>x</sub>, respectively)  
 6 in the model during July-August 2005. Results are calculated using 3-hourly model output. White  
 7 areas denote absolute values of  $O_3$ -CO correlation coefficients less than 0.2.

Deleted: ure